

# UNSUPERVISED REPRESENTATION LEARNING FOR 3D MESH PARAMETERIZATION WITH SEMANTIC AND VISIBILITY OBJECTIVES

AmirHossein Zamani<sup>1,2,3</sup> \* Bruno Roy<sup>1</sup> Arianna Rampini<sup>1</sup>

<sup>1</sup> Autodesk Research    <sup>2</sup> Mila – Quebec AI Institute    <sup>3</sup> Concordia University

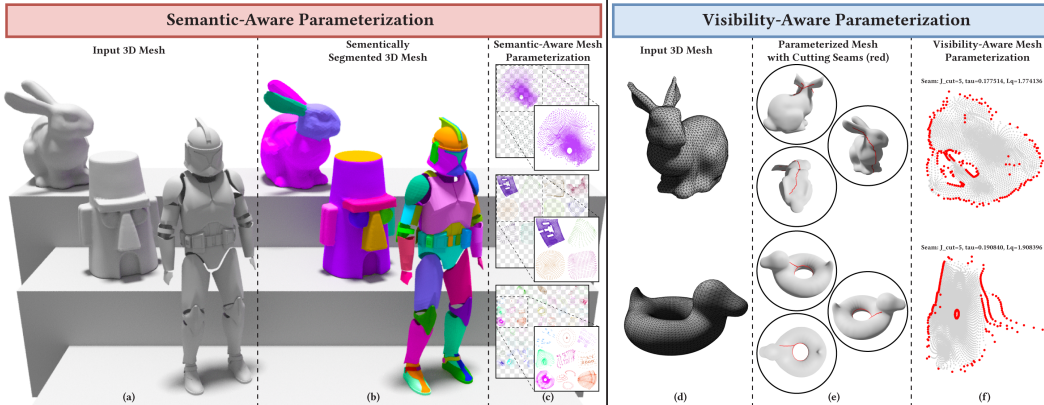


Figure 1: 3D mesh parameterizations generated by our proposed semantic- (left) and visibility-aware (right) pipelines. **Semantic-Aware (left - Sec. 3.3):** To encourage semantically coherent UV charts that simplify texture editing, given an input 3D mesh (a), we design a *partition-and-parameterize* strategy: (b) compute a per-vertex semantic partition of the mesh, (c) learn a geometry-preserving UV parameterization (Sec. 3.2) independently for each semantic part to obtain per-part UV islands, and then aggregate and pack these islands into a unified UV atlas (insets). **Visibility-Aware (right - Sec. 3.4):** To encourage seamless UV mappings, our visibility-aware pipeline (d) takes an input 3D mesh, jointly (e) guides cutting-seam placement (red curves), extracts the corresponding boundary points in UV space (red dots), and (f) estimates a global geometry-preserving parameterization. As a result, the method steers cutting seams toward less-visible (more occluded) surface regions, resulting in more visually seamless UV maps.

## ABSTRACT

Recent 3D generative models produce high-quality textures for 3D mesh objects. However, they commonly rely on the heavy assumption that input 3D meshes are accompanied by manual mesh parameterization (UV mapping), a manual task that requires both technical precision and artistic judgment. Industry surveys show that this process often accounts for a significant share of asset creation, creating a major bottleneck for 3D content creators. Moreover, existing automatic methods often ignore two perceptually important criteria: (1) semantic awareness (UV charts should align semantically similar 3D parts across shapes) and (2) visibility awareness (cutting seams should lie in regions unlikely to be seen). To overcome these shortcomings and to automate the mesh parameterization process, we present an unsupervised differentiable framework that augments standard geometry-preserving UV learning with semantic- and visibility-aware objectives. For semantic-awareness, our pipeline (i) segments the mesh into semantic 3D parts, (ii) applies an unsupervised learned per-part UV-parameterization backbone, and (iii) aggregates per-part charts into a unified UV atlas. For visibility-awareness, we use ambient occlusion (AO) as an exposure proxy and back-propagate a soft differentiable AO-weighted seam objective to steer cutting seams toward occluded regions. By conducting qualitative and quantitative evaluations against state-of-the-art methods, we show that the proposed method produces UV atlases that better support texture generation and reduce perceptible seam artifacts compared to recent baselines. Our implementation code is publicly available at: <https://github.com/AHHH975/Semantic-Visibility-UV-Param>.

\*Correspondence to: [amirhossein.zamani@mila.quebec](mailto:amirhossein.zamani@mila.quebec)

## 1 INTRODUCTION

Texture mapping, also called UV/Mesh parameterization, converts a 3D mesh surface into a 2D image (atlas) and is a core step in digital 3D content production, enabling texture synthesis, painting, transfer, and high-quality rendering. While recent 3D generative methods produce high-quality textures for 3D mesh objects, they commonly rely on the heavy assumption that input 3D meshes are accompanied by the mesh parameterization process that requires both technical precision and artistic judgment. This assumption limits usability for content creators and designers. Moreover, industry surveys show that this process often accounts for a significant share of asset creation, creating a major bottleneck for 3D content creators. To address these issues and automate mesh parameterization, numerous methods have been proposed that mainly focus on geometric properties such as bijectivity Tutte (1963); Sheffer et al. (2007a), conformality (angle-preservation) Lévy et al. (2023), stretch (length-preservation) Sander et al. (2002), and equiareality (area-preservation) Zou et al. (2011). While these properties are necessary to achieve a high-quality parameterization, they are not sufficient for many downstream applications in content creation and texture synthesis. In particular, two perceptual criteria are often neglected: (1) *semantic awareness*, 2D UV charts should align with semantically meaningful surface 3D parts so that textures designed for a semantic region remain coherent and transferable across 3D shapes; and (2) *visibility awareness*, seams should be placed where they are unlikely to be observed under typical viewpoints and lighting, so that seam artifacts are less perceptible after texturing and rendering. To the best of our knowledge, only limited work has explored these properties individually: semantic-aware UV mapping Vermandere et al. (2024); Mukherjee et al. (2024) and visibility-aware UV learning Weill-Duflos et al. (2023); Sheffer & Hart (2002); Ray et al. (2010). However, none of the existing approaches address both objectives simultaneously. To overcome these shortcomings, we present an unsupervised differentiable framework that augments standard geometry-preserving UV learning with semantic- and visibility-aware objectives. For semantic-awareness, our pipeline (i) segments the mesh into semantic 3D parts, (ii) applies an unsupervised learned per-part UV-parameterization backbone, and (iii) aggregates per-part charts into a unified UV atlas. For visibility-awareness, we use ambient occlusion (AO) Zhukov et al. (1998) as an exposure proxy and back-propagate a soft differentiable AO-weighted seam objective designed to steer cutting seams toward occluded regions. The proposed pipeline has two stages: (i) a neural surface-parameterization backbone enforces geometry-preserving properties, (ii) semantic-aware and visibility-aware modules provide task-specific (e.g., texture painting) guidance. The main contributions of this study are: (i) We propose an unsupervised, differentiable framework that jointly estimates geometry-preserving UV parameterizations while optimizing semantic- and visibility-aware objectives. (ii) We introduce two novel perceptual objectives that directly connect UV parameterization to texture synthesis: a semantic-aware objective that aligns 2D UV charts with semantically meaningful 3D surface parts, and a visibility-aware objective that places seams in less-visible regions to minimize seam artifacts.

## 2 RELATED WORK

**Traditional UV Parameterization.** These methods aim to flatten 3D surfaces to 2D while minimizing distortion and avoiding overlaps. Early conformal (angle-preserving) techniques such as LSCM Lévy et al. (2023) and ABF++ Sheffer et al. (2005) reduce angular distortion via global optimization or iterative angle adjustment. Many approaches also enforce bijectivity and bound distortion: bounded-distortion parameterization Sorkine et al. (2002) limits local stretch by cutting into patches, bijective free-boundary methods Smith & Schaefer (2015) avoid overlaps without fixing boundaries, and SLIM Rabinovich et al. (2017) scales these guarantees to large meshes. Optimizing cuts and chart segmentation also have been addressed: AutoCuts Poranne et al. (2017) and OptCuts Li et al. (2018) jointly optimize seams and UV parameterization to trade off distortion and chart count, while Seamster Sheffer & Hart (2002) and Seamless Liu et al. (2017) place seams to minimize visible texture artifacts by aligning them with features or low-visibility regions. Although classical algorithms provide the geometric foundation for UV mapping, they often treat these goals independently and rarely exploit higher-level objectives (e.g., semantic parts or visibility), which can limit final texture quality.

**Learning-Based UV Parameterization.** The existing methods for UV parameterization can be grouped by input representation: explicit (meshes and point clouds) Zhao et al. (2025); Zhang et al. (2024b); Srinivasan et al. (2024); Chen et al. (2022); Teimury et al. (2020); Oechsle et al. (2019); Knodt et al. (2023), implicit (NeRFs) Xu et al. (2024a); Xiang et al. (2021); Srinivasan et al. (2024); Guan et al. (2023); Das et al. (2022), and 3D-Gaussian-splatting-based methods Xu et al. (2024b). In this work, we focus on explicit (mesh) parameterization, which is widely used in industry. Mesh-

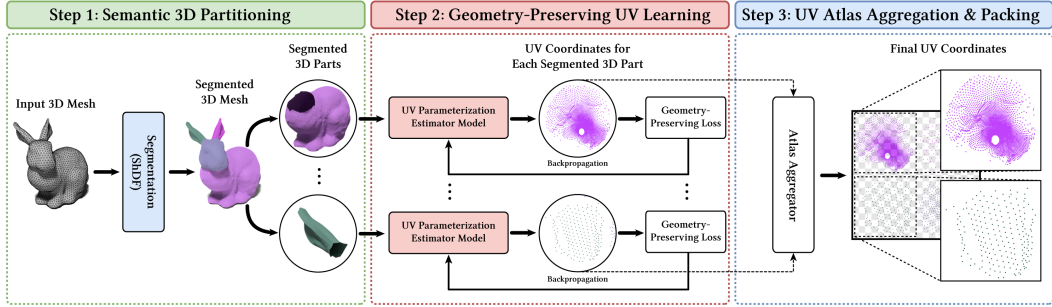


Figure 2: An overview of the training process of the proposed semantic-aware UV parameterization method (Sec. 3.3), consisting of three main stage: (i) *semantic 3D partitioning*, where we compute a per-vertex semantic partition of the input mesh using shape diameter function (Appendix A.1); (ii) *geometry-preserving UV learning*, where we apply the base UV-parameterization backbone (Sec. 3.2) independently to each semantic part to obtain per-part UV islands; and (iii) *UV atlas aggregation and packing* aggregate and pack these islands into a unified UV atlas.

based learning approaches Zhao et al. (2025); Srinivasan et al. (2024); Zhang et al. (2024a;b) usually train multi-layer perceptrons (MLPs) to learn UV mappings by optimizing three core criteria: (i) minimizing chart count, (ii) reducing distortion (preserving lengths, angles, and areas), and (iii) enforcing bijectivity via round-trip consistency. These MLPs are trained with carefully designed losses to satisfy those constraints. However, current learning-based methods often (i) *lack semantic awareness*, meaning that cutting seams are chosen only to reduce geometric distortion rather than to align with meaningful parts, and (ii) *ignore visibility when placing seams*, failing to steer cuts toward low-visibility regions and thus producing noticeable texture artifacts.

### 3 METHODOLOGY

We propose a two-stage, unsupervised, end-to-end differentiable framework to automatically learn 3D mesh parameterizations with semantic and visibility objectives. The training consists of two stages. In stage (i), *geometry-preservation mesh-parameterization learning* (Sec. 3.2), an MLP-based network is trained with fully differentiable geometric objectives defined in the UV domain to produce an initial UV mapping that satisfies low-distortion requirements. In stage (ii), *learning perceptual objectives* (Sec. 3.3 and Sec. 3.4), we introduce two perceptual objectives: *semantic awareness* and *visibility awareness*. By semantic awareness, we mean that the UV charts produced by stage (i) should align with semantically meaningful surface 3D parts. To this end, we adopt a *partition-and-parameterize* strategy based on the Shape Diameter Function Shapira et al. (2008): we first partition the input mesh into semantic 3D parts, learn a UV parameterization for each segmented part with the same MLP-based architecture used in stage (i), and finally aggregate the per-part UV charts into a single unified UV atlas. By visibility awareness, we mean that cutting seams should be placed on 3D mesh surface regions that are unlikely to be seen under typical viewpoints and lighting, making seam artifacts less perceptible after texturing. To this end, we propose a visibility-aware objective that uses ambient occlusion as a proxy for viewer exposure Zhukov et al. (1998), encouraging seam placement in regions of low exposure. An overview of the training procedure for *semantic awareness* and *visibility awareness* pipelines is shown in Fig. 2 and Algorithm 1, respectively.

#### 3.1 PROBLEM STATEMENT AND PRELIMINARIES

Given a 3D mesh  $M = (V, F)$  with vertex positions  $V \in \mathbb{R}^{N_v \times 3}$  (where  $N_v$  is the number of vertices), triangular faces  $F \in \mathbb{R}^{N_f \times 3}$  (where  $N_f$  is the number of faces), and per-vertex normals  $N \in \mathbb{R}^{N_v \times 3}$ , our goal is to learn a pointwise UV parameterization  $u_\theta : V \rightarrow \mathbb{R}^2$  that maps each vertex in  $V$  to a 2D coordinate, producing UV coordinates  $Q \in \mathbb{R}^{N_v \times 2}$  with row-wise correspondence between  $V$  and  $Q$ . We require the learned parameterization to satisfy the following properties during the learning process: (i) *geometry preservation*, i.e., the parameterization should be low-distortion and ideally preserve classical geometric properties such as (a) *isometry* (maintaining original edge lengths), (b) *equiareal* (preserving triangle/facet areas), and (c) *conformality* (preserving angles between edges); (ii) *UV-space efficiency and bijectivity*, the mapping should (a) efficiently utilize the available UV domain, (b) avoid overlapping projections of distinct 3D points, and (c) be one-to-one so that each surface point maps to a unique UV location; (iii) *high-quality cutting seams*, the parameterization should place seams in visually inconspicuous regions Weill-Duflos et al. (2023); Ray et al. (2010); Sheffer & Hart (2002); and (iv) *semantic awareness*, the UV mapping should semantically align 3D parts across different 3D mesh models to consistent regions in UV space to enable cross-shape correspondence Vermandere et al. (2024); Mukherjee et al. (2024); Cohen-Bar et al. (2025).

### 3.2 BASE NEURAL ARCHITECTURE FOR UV-PARAMETERIZATION LEARNING

To emulate the sequence of operations an artist would typically perform when constructing a UV atlas for a 3D mesh, such as stretching a canvas, placing it over the 3D surface, adding surface cuts where needed, and finally flattening it back to the plane, we build upon the idea of a deforming a 2D grid Yang et al. (2018) by leveraging *bi-directional cycle mapping* backbone, proposed in Zhang et al. (2024a;b); Srinivasan et al. (2024); Zhao et al. (2025). Intuitively, the bi-directional cycle mapping enforces that projecting a 3D surface patch into 2D UV coordinates and re-projecting those UVs back onto the 3D mesh yields the original data. Therefore, during the learning process, any seams, local stretches, distortions, or semantic misalignments show up as reconstruction errors. Then, by minimizing these errors, the model is guided to produce an approximately invertible and coherent parameterization that minimizes distortion. To build such a mapping, inspired by recent advances in global parameterization networks Zhao et al. (2025); Srinivasan et al. (2024), our backbone is composed of four geometrically interpretable subnetworks: (i) *deforming network*, which starts from a regular 2D grid and adaptively deforms it into candidate UV coordinates; (ii) *wrapping network*, which maps those 2D UV candidates to the 3D surface by smoothly bending the deformed grid to conform to the input mesh, bridging the 2D and 3D domains; (iii) *cutting network*, which operates on the wrapped 3D surface to open the closed geometry by placing seams that reduce distortion for subsequent flattening; and (iv) *unwrapping network*, which projects the resulting open 3D surface back to 2D while preserving smoothness and geometric coherence. In this design, Each subnetwork is a pointwise MLP applied to mesh vertices, and the whole architecture is trained end-to-end in an unsupervised fashion. The four subnetworks form two complementary branches enforcing 2D–3D–2D and 3D–2D–3D cycles for ensuring consistency across 2D and 3D domains. Coupled with differentiable losses that encourage bijectivity and minimize distortion, this backbone produces candidate UV parameterizations for the next stages. Further details on the loss design and the interaction of the four sub-networks within the two-branch bi-directional cycle are given in Appendix A.2.

### 3.3 SEMANTIC-AWARE UV PARAMETERIZATION

The UV parameterization, obtained from the *bi-directional cycle mapping*, is used in the next step, *semantic-aware UV parameterization*. To encourage semantically coherent UV charts that simplify texture editing, transfer, and cross-object correspondence, we design a *partition-and-parameterize* pipeline (illustrated in Fig. 2). Our semantic-aware parameterization has three stages: (i) compute a per-vertex semantic partition of the input mesh using the shape diameter function (ShDF) Shapira et al. (2008); (ii) apply the base UV-parameterization backbone from Sec. 3.2 independently to each semantic 3D part to obtain per-part UV islands; and (iii) aggregate and pack these islands into a unified UV atlas. We now describe each stage in detail.

**3D Partitioning using Shape Diameter Function.** Given an input mesh  $\mathcal{M} = (V, F)$ , we compute a semantic partition  $S : V \rightarrow \{1, \dots, K\}$  using the shape diameter function (ShDF) Shapira et al. (2008) as our primary signal. Intuitively, the ShDF maps each surface sample to a scalar that estimates the local object thickness (the diameter of the object in the vicinity of that sample). Similar ShDF values typically indicate coherent semantic parts (e.g., limbs, body, handles), making the ShDF a practical cue for part-level partitioning of 3D shapes. Specifically, our 3D partitioning strategy consists of the following steps (See Appendix. A.1 for the detailed explanation of each step): (i) *compute local ShDF*, we compute a local thickness (ShDF) per face via ray casting inside a cone about the inward normal at each surface point and smoothing the samples for spatial coherence; (ii) *fit GMM*, to obtain soft per-face class likelihoods, we use a 1-D Gaussian mixture model (GMM) to fit  $K$  (the desired number of semantic components) Gaussians to the per-face thicknesses; (iii) *boundary smoothness cost*, to bias the partition toward spatially coherent regions, we then combine these likelihoods with a geometry-aware pairwise smoothness penalty (e.g., a dihedral-angle based boundary cost) on adjacent faces on the geometry to encourage coherent regions and penalize label changes across sharp edges. (iv) *initial labeling*, we then assign each face to the GMM component with maximum probability (minimum negative log-likelihood). This produces a purely data-driven segmentation that is generally noisy but captures the major mode structure of the thickness field. (v) *refine with graph cuts*, we then refine the initial assignment by minimizing a global energy (see Eq. 10 in Appendix A.1) via iterative alpha-expansion, solving each expansion by an optimal min-cut. Repeating this process across labels and iterating a few times yields stable and low-energy 3D partitions. (vi) *Relabel connected components*, after refinement, a single label index can correspond to multiple disconnected components. To solve this issue, we relabel each connected component of faces so that every final label corresponds to a single connected sub-mesh. This guarantees that sub-

sequent per-part processing operates on contiguous regions. (vii) *Post-processing*, to produce clean 3D segmentation results, we apply several simple post-processing heuristics to remove spurious tiny components that would complicate per-part UV parameterization. The output is then a set of connected semantic sub-meshes  $\{\mathcal{M}_k = (V_k, F_k)\}_{k=1}^K$  suitable for the per-part UV parameterization stage described in Sec.3.2. This high-level pipeline is simple, robust, and fast. Full algorithmic and implementation details are provided in Appendix A.1 for reproducibility. We also evaluate a modern zero-shot segmentation baseline, SAMesh Tang et al. (2024), as an alternative partitioner and report comparative results in our ablation study.

---

**Algorithm 1** Visibility-Aware UV Parameterization Training
 

---

**Require:** Mesh  $\mathcal{M} = (V, F)$  with edges  $E$ , vertices  $V \in \mathbb{R}^{N_v \times 3}$ , normals  $N \in \mathbb{R}^{N_v \times 3}$ , faces  $F \in \mathbb{Z}^{N_f \times 3}$ , per-vertex AO  $\in \mathbb{R}^{N_v}$ , iterations  $T$ , and model weights  $\theta$

1: **for**  $t = 1$  to  $T$  **do**

2:   # Step 1: Learning Mesh Parameterization  
 3:    $Q \leftarrow \text{UV\_Backbone}(G, P)$  # forward pass  
 4:    $Q_n \leftarrow \text{normalization}(Q)$  # Norm. UVs  
 5:    $\mathcal{L}_{\text{wrap}} \leftarrow \text{Chamfer}(\tilde{P}, P)$  # wrap loss Eq. 16  
 6:    $L_{\text{unwrap}} \leftarrow \text{Rep}(Q_n)$  # Rep. loss Eq. 18

7:   Cycle-consistency loss (Eq. 17):

$$\mathcal{L}_{\text{cycle.p}} := \|\hat{Q} - \hat{Q}_{\text{cycle}}\|^2 + \|P - \tilde{P}\|^2, \\ L_{\text{cc.n}} := \text{CosSim}(P_n, P_{cn})$$

8:    $e_1, e_2 \leftarrow \text{Compute\_Differential\_Properties}(P_c, Q)$   
 9:    $L_{\text{dist}} \leftarrow L_{\text{DDL}}(e_1, e_2) + L_{\text{TDL}}(Q, V, F)$  # Eq. 19  
 10:   Set base loss (Eq. 15):

$$L_{\text{base}} \leftarrow L_{\text{wrap}} + 0.01 L_{\text{unwrap}} + 0.01 L_{\text{cc.p}} + \\ 0.005 L_{\text{cc.n}} + 0.01 L_{\text{conf.diff}} + 10^{-5} L_{\text{conf.tri}}$$

11:   # Step 2: Optimizing Surface Cuts  
 12:   Differentiable neighbor selection (Eq. 5):  
 $\eta_i \leftarrow \frac{1}{\gamma} \log \left( \sum_{j \in \mathcal{N}_i^{\text{cut}}} \exp(\gamma \|q_i - q_{i,j}\|_2) \right)$   
 13:   Differentiable seam extraction (Eq. 5):  
 $s_i \leftarrow \sigma(\beta(\eta_i - \tau))$   
 14:   Compute AO values (Eq. 4):  
 $\text{AO}(p) = \frac{1}{\pi} \int_{\Omega+(p)} V(p, \omega) (n(p) \cdot \omega) d\omega$   
 15:    $S \leftarrow \sum_{i \in V} s_i + \epsilon$   
 16:    $L_{\text{AO}} \leftarrow \frac{1}{S} \sum_{i \in V} s_i \cdot \text{AO}_i$  # seam loss (Eq. 7)  
 17:    $L_{\text{vis}} \leftarrow L_{\text{base}} + 0.004 \cdot L_{\text{AO}}$  # visibility loss (Eq. 8)  
 18:    $g \leftarrow \nabla_{\theta} L_{\text{vis}}(\theta)$   
 19:    $\theta \leftarrow \theta - \eta g$

20: **end for**  
 21: **return**  $\theta$

---

our current aggregator is intentionally simple and deterministic: the final UV sheet is a unit square subdivided into a  $G \times G$  regular grid, where  $G = \lceil \sqrt{K} \rceil$ . We then assign each part  $k$  a unique grid cell indexed by row and column  $(r_k, c_k)$  in row-major order. Each normalized island  $Q_k$  is placed into its assigned cell via a uniform similarity transform (scale  $s$  and translation  $t_{r_k, c_k}$ ):

$$T_k(u) = s \cdot u + t_{r_k, c_k}, \quad s = \frac{1 - 2 \cdot \text{pad}}{G}, \quad t_{r,c} = \left[ \frac{c + \text{pad}}{G} \quad \frac{r + \text{pad}}{G} \right]^T, \quad (2)$$

where  $\text{pad} \in [0, 0.5)$  is a small margin (in normalized UV units) to prevent bleeding between neighboring cells. Using the same scale  $s$  for all charts enforces a consistent texel density across parts, which simplifies texture baking and editing workflows. The final per-vertex UV for the whole mesh is therefore

$$u_{\text{final}}(v) = T_k(u_{\theta_k}(v)), \quad v \in V_k. \quad (3)$$

The grid-based aggregator is simple, deterministic, and effective for per-part editing and texture transfer, and can be replaced by more advanced packing solvers (heuristic or optimization-based)

**Per-part Parameterization.** For each semantic submesh  $\mathcal{M}_k$ , obtained from previous step, we instantiate the base parameterization backbone, described in Sec. 3.2 and Appendix A.2, and optimize a part-specific mapping  $u_{\theta_k} : V_k \rightarrow \mathbb{R}^2$ . Each part is trained with the same suite of differentiable objectives used for the global model. Therefore, we minimize the per-part loss

$$\mathcal{L}_{\text{part}}^{(k)}(\theta_k) = \mathcal{L}_{\text{wrap}}^{(k)} + \mathcal{L}_{\text{cycle}}^{(k)} + \mathcal{L}_{\text{repel}}^{(k)} + \mathcal{L}_{\text{dist}}^{(k)} \quad (1)$$

where  $\mathcal{L}_{\text{wrap}}^{(k)}$ ,  $\mathcal{L}_{\text{cycle}}^{(k)}$ ,  $\mathcal{L}_{\text{repel}}^{(k)}$ , and  $\mathcal{L}_{\text{dist}}^{(k)}$  denote the wrapping objective (Eq. 16), cycle-consistency regularizer (Eq. 17), anti-overlap penalty (Eq. 18), and distortion penalty (Eq. 19), respectively (see Appendix A.2 for definitions); each term is evaluated on the submesh  $\mathcal{M}_k$ . To minimize Eq. 1, we compute the gradient  $\nabla_{\theta_k} \mathcal{L}_{\text{part}}^{(k)}(\theta_k)$  for the bi-directional cycle mapping subnetwork of part  $k$  and apply a gradient-descent update using  $\theta_k \leftarrow \theta_k - \eta \nabla_{\theta_k} \mathcal{L}_{\text{part}}^{(k)}(\theta_k)$  where  $\eta$  is the learning rate. This yields  $K$  independently trained bi-directional sub-networks (one per semantic 3D part produced by our ShDF segmentation). The resulting per-part parameterizations are then passed to the aggregation-and-packing stage to form a unified UV atlas. Training parts independently allows each semantic region to adopt a chart that best trades off local geometric fidelity and developability.

**Atlas Aggregation and Packing.** After optimizing all parts, we obtain per-part UV islands  $\{Q_k \subset [0, 1]^2\}_{k=1}^K$  (each normalized to the unit square) corresponding to each 3D segmented part. These islands are merged into a single atlas by an *atlas aggregator*. For clarity and reproducibility

without changing the per-part losses in Eq. 1. Overall, the proposed *partition-and-parameterize* design preserves the geometry-focused objectives of Sec. 3.2 while producing semantically organized UV atlases that are easier to edit and use for correspondence.

### 3.4 VISIBILITY-AWARE UV PARAMETERIZATION

A common perceptual failure of UV atlases is that seams positioned on exposed, well-lit, or frequently viewed regions create visible discontinuities once textures are applied.

To address this, we introduce a *visibility-aware* objective that biases seam placement toward surface areas with low viewer exposure. As a proxy for visibility, we leverage *ambient occlusion* (AO) Zhukov et al. (1998), a standard geometric measure of how much of the local hemisphere around a surface point is blocked by nearby geometry Landis (2002); Christensen (2002); Bavoil & Sainz (2008); McGuire (2010); Laine & Karras (2010); Méndez-Feliu & Sbert (2009). Our training procedure consists of four steps: (i) compute per-vertex AO values on the input mesh, (ii) apply the base UV-parameterization backbone (Sec. 3.2) to obtain candidate UV islands, (iii) extract UV boundary points corresponding to cutting seams, and (iv) compute and minimize the AO-weighted average over the associated 3D vertices. This objective guides the backbone to produce UV islands whose seams coincide with regions of low exposure, thereby relocating cuts to less visible areas of the 3D surface and reducing perceptible seam artifacts after texturing and rendering. We now detail each step in turn.

#### Compute Per-Vertex Ambient Occlusion.

Let  $p$  be a point on the surface with unit normal  $n(p)$ . Define the hemisphere of outgoing directions as  $\Omega^+(p) = \{\omega \in \mathbb{S}^2 : n(p) \cdot \omega > 0\}$ . The binary visibility function  $V(p, \omega) = \begin{cases} 1, & \text{if the ray starting at } p \text{ in direction } \omega \text{ does not intersect the surface (unoccluded)} \\ 0, & \text{otherwise (occluded)} \end{cases}$  measures

whether direction  $\omega$  is visible from  $p$ . The ambient-occlusion exposure  $AO(p) \in [0, 1]$  is then defined as the cosine-weighted average visibility over the hemisphere  $\Omega^+(p)$ :

$$AO(p) = \frac{1}{\pi} \int_{\Omega^+(p)} V(p, \omega) (n(p) \cdot \omega) d\omega. \quad (4)$$

By this convention,  $AO(p) = 1$  indicates a fully exposed point (no occlusion) and  $AO(p) = 0$  indicates a fully occluded point. In practice AO is estimated by Monte Carlo hemisphere sampling Veach (1998) or by high-quality offline ray sampling Pharr et al. (2023) for evaluation. In our implementation, we compute ambient occlusion using the libigl geometry processing library Jacobson et al. (2018), leveraging its mesh-based AO utilities for efficient per-vertex AO estimation.

**Learning Mesh Parameterization.** Once per-vertex AO values are computed, we generate the UV parameterization using the base backbone described in Sec. 3.2 and Appendix. A.2 to obtain a potential UV parameterization candidate.

**Cutting Seam Extraction in UV Space.** We then extract cutting seams directly from the UV mapping learned in the previous step. This process has three steps: (i) *neighbor selection*, given a set of 3D surface points  $P$  with their corresponding UV coordinates  $Q$ , the method determines whether each vertex lies on a seam by exploring its neighborhood. For each 3D point  $p_i \in P$  with UV coordinate  $q_i \in Q$ , we first find its  $N$  nearest neighbors in 3D, denoted  $\{p_{i,j}\}_{j=1}^N$ , with corresponding UV coordinates  $\{q_{i,j}\}_{j=1}^N$ . (ii) *differentiable max UV distance computation*, we then (similar to Zhao et al. (2025)) compute the maximum UV distance between  $q_i$  and its neighbors:

$$\eta_i = \max(\|q_i - q_{i,j}\|_2)_{j=1}^N \quad (5)$$

Next, we define a threshold  $\tau$  based on the UV domain size. Specifically, we compute the bounding square of the UV map with side length  $L(Q)$ , and set  $\tau = \tau_{\text{scale}} \cdot L(Q)$  where  $\tau_{\text{scale}}$  is a constant

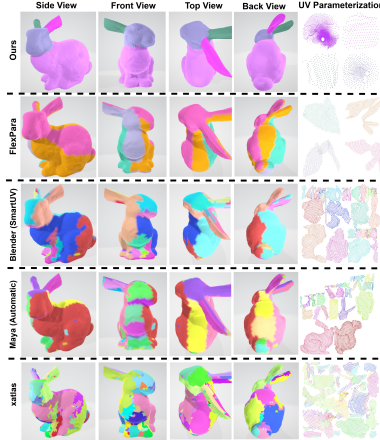


Figure 3: Qualitative results of the proposed semantic-aware UV parameterization method on a Rabbit mesh. For each method, we show the rendered 3D object from multiple viewpoints, with the corresponding UV atlas in the right-most column. As shown, our method produces UV charts that are align more semantically with the mesh’s 3D semantic parts, unlike the baselines.

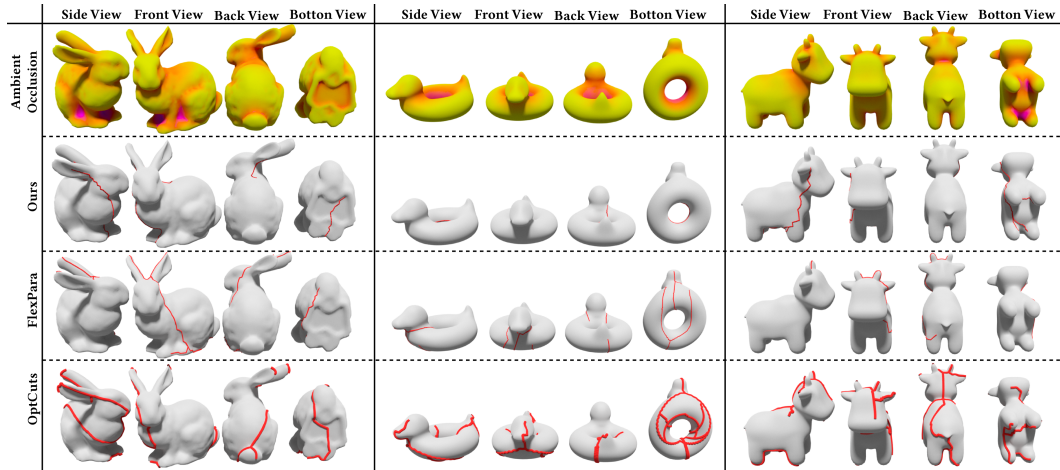


Figure 4: Qualitative results for visibility-aware seam placement and UV parameterization on three representative meshes. For each mesh, the top row shows per-vertex ambient occlusion (yellow = exposed, purple = occluded). Beneath are the visualizations of cutting seams (red) from our method, FlexPara Zhao et al. (2025), and OptCuts Li et al. (2018) (top to bottom). Our method places a larger fraction of seam geometry in less-exposed regions, reducing the likelihood of visible seam artifacts under typical viewpoints.

(e.g., 0.1 by default). However, this maximization is not inherently differentiable, so we introduce mathematical modifications to ensure differentiability during the learning process. Specifically, instead of a hard decision, we assign each vertex a differentiable *soft seam membership* score:  $s_i = \sigma(\beta(\eta_i - \tau))$  where  $\sigma(\cdot)$  is the sigmoid function and  $\beta$  controls the sharpness of the transition. The maximization problem can then be formulated as a differentiable function:

$$\eta_i \approx \frac{1}{\gamma} \log \left( \sum_{j \in \mathcal{N}_i^N} \exp(\gamma \|q_i - q_{i,j}\|_2) \right), \quad s_i = \sigma(\beta(\eta_i - \tau)), \quad \tau = \tau_{\text{scale}} L(Q) \quad (6)$$

where  $\mathcal{N}_i^N$  denotes the  $N$  nearest 3D neighbors in the 1-ring of vertex  $i$ , and  $\gamma, \beta, \tau_{\text{scale}}$  control the soft-max / sigmoid sharpness and threshold scale. With this formulation, vertices with  $s_i$  close to 1 are highly likely to lie on seams, while vertices with  $s_i$  near 0 are not. This procedure produces a soft mask  $s \in [0, 1]^V$  that marks the cutting seams in UV space and is used in the next step to compute the ambient occlusion loss on the seam vertices.

**Visibility-Aware Seam Loss.** After identifying soft seam memberships  $s_i \in [0, 1]$  for each vertex  $v_i$ , we encourage seams to lie in less visible regions of the surface. As a visibility proxy, we use per-vertex ambient occlusion values  $AO_i \in [0, 1]$ , computed in the first step, where 0 indicates fully visible and 1 indicates fully occluded. The loss is defined as the weighted average of occlusion values, using soft seam memberships as weights:

Table 1: Quantitative comparison of the proposed visibility-aware UV parameterization method against baselines on multiple evaluation metrics.

Method	Visibility ↓	Conformality ↑	Equiareality ↑	Time (s) ↓
OptCuts Li et al. (2018)	0.7855	<b>0.9341</b>	<b>0.8934</b>	240
FlexPara (Single-Chart) Zhao et al. (2025)	0.8604	0.9097	0.6759	2
Ours - Visibility-Aware Param	<b>0.6065</b>	0.9175	0.6093	2
Ours - Semantic+Visibility-Aware Param	0.6534	0.9153	0.6369	15

$$\mathcal{L}_{\text{AO}} = \frac{\sum_i s_i AO_i}{\sum_i s_i + \varepsilon} \quad (7)$$

where  $\varepsilon$  is a small constant to avoid division by zero. Intuitively, if the network assigns high seam weight  $s_i$  to highly visible vertices (low  $AO_i$ ), the loss is large. Conversely, assigning seam weight to occluded vertices (high  $AO_i$ ) reduces the loss. Therefore, minimizing  $\mathcal{L}_{\text{AO}}$  guides seam placement toward regions of low exposure.

**Integration with The Backbone Losses.** To jointly optimize geometric and visibility properties, we augment the visibility-aware seam loss  $\mathcal{L}_{\text{AO}}$  with the backbone objective from Sec. 3.2 and Appendix. A.2. The full visibility-aware objective is then becomes

$$\mathcal{L}_{\text{vis}}(\theta) = \mathcal{L}_{\text{wrap}} + \mathcal{L}_{\text{cycle}} + \mathcal{L}_{\text{repel}} + \mathcal{L}_{\text{dist}} + \lambda_{\text{vis}} \mathcal{L}_{\text{AO}} \quad (8)$$

where  $\mathcal{L}_{\text{wrap}}$ ,  $\mathcal{L}_{\text{cycle}}$ ,  $\mathcal{L}_{\text{repel}}$ , and  $\mathcal{L}_{\text{dist}}$  denote the wrapping objective (Eq. 16), cycle-consistency regularizer (Eq. 17), anti-overlap penalty (Eq. 18), and distortion penalty (Eq. 19), respectively (see Appendix A.2 for definitions). To minimize Eq. 8, we compute the gradient  $\nabla_{\theta} \mathcal{L}_{\text{vis}}(\theta)$  for the bi-directional cycle mapping network, and then apply a gradient-descent update using  $\theta \leftarrow \theta - \eta \nabla_{\theta} \mathcal{L}_{\text{vis}}(\theta)$  where  $\eta$  is the learning rate.

## 4 EXPERIMENTS AND RESULTS

We evaluate our unsupervised semantic- and visibility-aware UV parameterization pipelines on a diverse collection of meshes and compare against several baselines. We provide both qualitative and quantitative comparisons to: FlexPara Zhao et al. (2025) (recent state-of-the-art global parameterization network), Autodesk Maya Autodesk, Inc. (2025) (industry-grade commercial software), Blender Blender Foundation (2025) (popular open-source modeling tool), and xatlas jpcy (2025) (widely-used C++ library for generating unique texture coordinates suitable for lightmap baking and texture painting). Figs. 1, 3, 4, and 5 show representative qualitative results, and Tables. 1 and 2 presents quantitative results of our semantic-aware and visibility-aware pipelines against baselines (additional results are provided in Appendix A.3). In the following, we detail each experiment and its corresponding results.

**Comparative Evaluation of Semantic-Aware UV Parameterization.** To evaluate the performance of the proposed semantic-aware UV parameterization pipeline, we compare our method against FlexPara Zhao et al. (2025), Autodesk Maya’s Automatic UV generator Autodesk, Inc. (2025), Blender’s SmartUV Blender Foundation (2025), and xatlas jpcy (2025). Fig. 3 shows a representative comparison on a single Bunny mesh; additional results on more diverse and complex meshes are provided in Figs. 11 and 12 in Appendix A.3.

In Fig. 3 and Fig. 11, each row corresponds to one method. Semantic parts are color-coded, and columns show the rendered 3D mesh from multiple camera viewpoints. The rightmost column depicts the unwrapped UV coordinates, where UV islands are color-coded consistently with their corresponding semantic 3D parts in the rendered views. As shown, our method successfully identifies semantic parts of the input mesh, parameterizes them, and maps them into UV space with low distortion. This leads to cleaner, more interpretable charts that directly benefit downstream tasks such as texture painting and transfer. By contrast, the baseline methods fail to consistently capture and parameterize semantic parts of the 3D mesh.

**Comparative Evaluation of Visibility-Aware UV Parameterization.** To evaluate the performance of the proposed visibility-aware UV parameterization pipeline, we compare our method against FlexPara Zhao et al. (2025) and OptCuts Li et al. (2018). Figs. 4 and 8 present representative comparisons on different meshes. Additional examples appear in Figs. 5, 9, and 10 in Appendix A.3. In Fig. 4 the top row visualizes per-vertex ambient occlusion (AO): lighter tones (e.g., yellow) indicate high exposure (more visible) while darker tones (e.g., purple) indicate low exposure (more occluded). A desirable parameterization therefore places cutting seams on darker, less-visible regions to reduce perceptible seam artifacts after texturing and rendering. The rows beneath show UV parameterizations produced by our method, FlexPara, and OptCuts (in that order). Qualitatively, our method allocates a larger fraction of seam geometry to low-exposure regions compared to the baselines. Table 1 (and Fig. 7 in Appendix A.3) quantitatively supports this observation: the report the mean AO values of seam vertices for each method, where lower scores indicate seams located in less-visible (more occluded) areas. As shown, our method consistently attains lower mean seam-AO, confirming that the visibility-aware objective successfully biases seam placement toward less-exposed surface regions. Also, Fig. 5 illustrates checkerboard texturing on different mesh objects using parameterizations from our method and from baselines. As shown, our method produces noticeably more seamless texture patterns when rendered from visible viewpoints, whereas FlexPara and OptCuts exhibit prominent cutting seams (highlighted in the zoomed-in insets of Fig. 5).

**Quantitative Comparison.** We quantitatively evaluate both the semantic-aware and visibility-aware components of our pipeline on a collection of representative meshes. For the semantic-aware

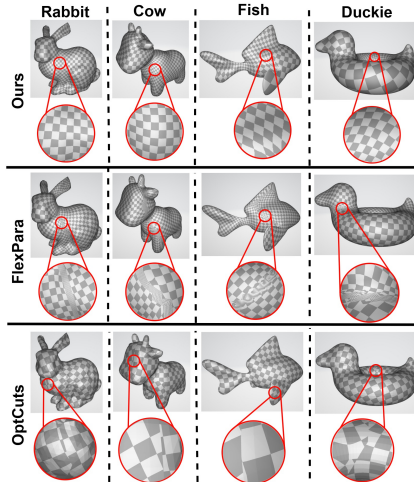


Figure 5: Checkerboard texturing comparison using UV parameterizations produced by our visibility-aware method, FlexPara Zhao et al. (2025), and OptCuts Li et al. (2018). Each row shows rendered views of different meshes textured with a checkerboard and a magnified inset of a visually important region near seams (red circles). Because our method steers seams toward occluded regions, the checkerboard pattern appears substantially more continuous from typical camera viewpoints. By contrast, baselines exhibit visible seam artifacts in the zoomed-in insets.

pipeline we report (i) *Hamming distance* (lower is better), the fraction of vertices whose labels disagree after optimal label matching to the reference (we use SAMesh Tang et al. (2024) outputs as a ground-truth); and (ii) *Rand Index (RI)* (higher is better), a pairwise agreement measure that counts how often vertex pairs are grouped or separated identically between the two labelings. For the *visibility-aware* pipeline we report *Mean seam AO* (lower is better in our AO convention, where 0 = occluded and 1 = exposed), the average ambient-occlusion value over seam vertices, which indicates how well seams are placed in occluded regions. In addition to these task-specific metrics, we evaluate geometric quality for all methods using *conformality (angle-preservation)* and *equiareality (area-preservation)* (higher is better) to ensure the parameterizations remain faithful to the original surface. Tables 1 and 2 summarize these metrics and compare our method against the baselines described in Sec. 4. Further discussion of the results in these two tables are provided in Appendix A.3.

**Ablation Studies.** To understand which design choices drive our results, we perform a set of controlled ablations and summarize the key findings below (additional qualitative examples are in Fig. 13 and Fig. 14 in Appendix A.3).

(i) *Partitioning strategy (ShDF vs. SAMesh)*. We replace our default Shape Diameter Function (ShDF) partitioner Shapira et al. (2008) with SAMesh Tang et al. (2024) while keeping the remainder of the *partition-and-parameterize* pipeline identical. Qualitatively both partitioners produce part decompositions that align with geometric structure across simple and complex models, resulting compact, low-distortion per-part UV charts (see the appendix Fig. 13 and Fig. 14).

Quantitatively (Table 4 in Appendix. A.3), using ShDF in our pipeline yields UV parameterizations that are more conformal (better angle preservation) and more equiareal (better area preservation) than those produced when using SAMesh. (ii) *Visibility loss (with vs. without)*. We ablate the proposed visibility-aware objective (Sec. 3.4) by training identical models with and without  $\mathcal{L}_{vis}$ . The visibility-aware objective consistently lowers the mean AO of seam vertices (Fig 6), i.e., it moves seams to regions of lower exposure (lower AO values). Qualitatively, models trained with the AO loss produce seams that are less salient in rendered images from canonical viewpoints (see Fig. 5). Importantly, as presented in Table. 1, adding the visibility term does not noticeably degrade geometric distortion metrics, conformality (angle-preservation) and equiareality area-preservation). The ablations show that: (i) the ShDF partitioner is a semantically reliable and geometry-driven initializer for our semantic-aware parameterization across diverse shapes; and (ii) the visibility-aware loss is required to effectively move seams to less-exposed regions without harming geometric quality. Additional ablation studies are provided in Appendix A.3.

## 5 CONCLUSIONS

This study presents an unsupervised representation-learning framework for semantic- and visibility-aware UV parameterization of 3D meshes. The semantic-aware pipeline leverages high-level mesh partitioning to align UV islands with meaningful 3D parts, producing UV charts that are easier to interpret and manipulate for downstream tasks such as texture synthesis. The visibility-aware pipeline uses ambient occlusion as a differentiable proxy for visual exposure to guide seam placement toward less-visible regions, reducing perceptual artifacts in texturing and rendering. Extensive qualitative and quantitative comparisons to state-of-the-art methods show our parameterizations achieve low distortion, stronger semantic alignment, and seams placed in perceptually favorable locations. We expect these contributions to serve as building blocks for generative 3D models and broader 3D content creation. Therefore, future work includes jointly learning UV parameterization and texture generation.

Table 2: Quantitative comparison of the proposed semantic-aware UV parameterization method against baselines on multiple evaluation metrics.

Method	Semantic Awareness		Conformality $\uparrow$	Equiareality $\uparrow$	Inference Time (sec) $\downarrow$
	Hamming Distance $\downarrow$	Rand Index $\uparrow$			
xatlas jpcy (2025)	0.8896	0.7023	<b>0.9792</b>	<b>0.9341</b>	12
Blender Blender Foundation (2025)	0.8634	0.7173	0.9289	0.9023	< 1
Maya Autodesk, Inc. (2025)	0.8615	0.7125	0.9272	0.8746	< 1
FlexPara (Multi-Chart) Zhao et al. (2025)	0.5980	0.6902	0.9592	0.7606	2
Ours - Semantic-Aware Param	<b>0.3188</b>	<b>0.8151</b>	0.9123	0.6707	15
Ours - Semantic+Visibility-Aware Param	0.3212	0.8087	0.9153	0.6369	15

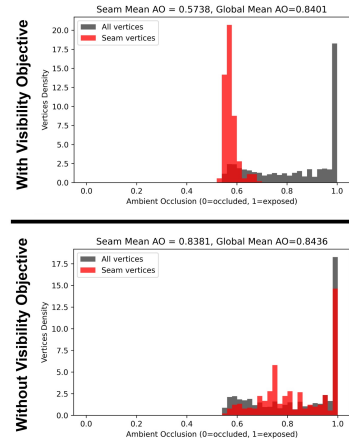


Figure 6: Ablation: Quantitative distribution of seam vertices ambient occlusion for meshes parameterized by using our proposed method, FlexPara Zhao et al. (2025), and OptCuts Li et al. (2018).

## ACKNOWLEDGMENTS

This research was supported by Autodesk Research and the Autodesk AI Lab. We are especially thankful for the collaborative environment, technical resources, and insightful discussions that contributed to shaping this work.

## REFERENCES

- Autodesk, Inc. *Autodesk Maya (Version 2025.x)*. Autodesk, Inc., 2025. URL <https://www.autodesk.com/products/maya/overview>. Accessed: 2025-09-11.
- Louis Bavoil and Miguel Sainz. Screen space ambient occlusion. *NVIDIA developer information: http://developers.nvidia.com*, 6(2):6, 2008.
- Blender Foundation. *Blender – a 3D creation suite (Version 4.5)*. Blender Foundation, 2025. URL <https://www.blender.org>. Accessed: 2025-09-11.
- Zhiqin Chen, Kangxue Yin, and Sanja Fidler. Auv-net: Learning aligned uv maps for texture transfer and synthesis. In *Proceedings of the IEEE/CVF conference on computer vision and pattern recognition*, pp. 1465–1474, 2022.
- Per H Christensen. Note# 35: Ambient occlusion, image-based illumination, and global illumination. *PhotoRealistic RenderMan Application Notes*, 2002.
- Dana Cohen-Bar, Daniel Cohen-Or, Gal Chechik, and Yoni Kasten. Tritex: Learning texture from a single mesh via triplane semantic features. In *Proceedings of the Computer Vision and Pattern Recognition Conference*, pp. 21403–21413, 2025.
- Sagnik Das, Ke Ma, Zhixin Shu, and Dimitris Samaras. Learning an isometric surface parameterization for texture unwrapping. In *European Conference on Computer Vision*, pp. 580–597. Springer, 2022.
- Michael S Floater and Kai Hormann. Surface parameterization: a tutorial and survey. *Advances in multiresolution for geometric modelling*, pp. 157–186, 2005.
- Yanran Guan, Andrei Chubarau, Ruby Rao, and Derek Nowrouzezahrai. Learning neural implicit representations with surface signal parameterizations. *Computers & Graphics*, 114:257–264, 2023.
- Kai Hormann, Bruno Lévy, and Alla Sheffer. Mesh parameterization: Theory and practice. 2007.
- Alec Jacobson, Daniele Panozzo, et al. libigl: A simple C++ geometry processing library, 2018. <https://libigl.github.io/>.
- jpcy. xatlas: Mesh parameterization / uv unwrapping library. <https://github.com/jpcy/xatlas>, 2025. Accessed: 2025-09-11.
- Julian Knodt, Zherong Pan, Kui Wu, and Xifeng Gao. Joint uv optimization and texture baking. *ACM Transactions on Graphics*, 43(1):1–20, 2023.
- Samuli Laine and Tero Karras. Two methods for fast ray-cast ambient occlusion. In *Computer Graphics Forum*, volume 29, pp. 1325–1333. Wiley Online Library, 2010.
- Hayden Landis. Production-ready global illumination. *Siggraph course notes*, 16(2002):11, 2002.
- Bruno Lévy, Sylvain Petitjean, Nicolas Ray, and Jérôme Maillot. Least squares conformal maps for automatic texture atlas generation. In *Seminal Graphics Papers: Pushing the Boundaries, Volume 2*, pp. 193–202. 2023.
- Minchen Li, Danny M Kaufman, Vladimir G Kim, Justin Solomon, and Alla Sheffer. Optcuts: Joint optimization of surface cuts and parameterization. *ACM transactions on graphics (TOG)*, 37(6): 1–13, 2018.

- Songrun Liu, Zachary Ferguson, Alec Jacobson, and Yotam I Gingold. Seamless: seam erasure and seam-aware decoupling of shape from mesh resolution. *ACM Trans. Graph.*, 36(6):216–1, 2017.
- Morgan McGuire. Ambient occlusion volumes. In *Proceedings of the 2010 ACM SIGGRAPH symposium on Interactive 3D Graphics and Games*, pp. 1–1, 2010.
- Àlex Méndez-Feliu and Mateu Sbert. From obscurances to ambient occlusion: A survey. *The Visual Computer*, 25(2):181–196, 2009.
- Anirban Mukherjee, Venkat Suprabath Bitra, Vignesh Bondugula, Tarun Reddy Tallapureddy, and Dinesh Babu Jayagopi. Semuv: Deep learning based semantic manipulation over uv texture map of virtual human heads. In *International Conference on Computer Vision and Image Processing*, pp. 112–127. Springer, 2024.
- Alessandro Muntoni and Paolo Cignoni. PyMeshLab, January 2021.
- Michael Oechsle, Lars Mescheder, Michael Niemeyer, Thilo Strauss, and Andreas Geiger. Texture fields: Learning texture representations in function space. In *Proceedings of the IEEE/CVF international conference on computer vision*, pp. 4531–4540, 2019.
- Matt Pharr, Wenzel Jakob, and Greg Humphreys. *Physically based rendering: From theory to implementation*. MIT Press, 2023.
- Roi Poranne, Marco Tarini, Sandro Huber, Daniele Panozzo, and Olga Sorkine-Hornung. Autocuts: simultaneous distortion and cut optimization for uv mapping. *ACM Transactions on Graphics (TOG)*, 36(6):1–11, 2017.
- Michael Rabinovich, Roi Poranne, Daniele Panozzo, and Olga Sorkine-Hornung. Scalable locally injective mappings. *ACM Transactions on Graphics (TOG)*, 36(4):1, 2017.
- Nicolas Ray, Vincent Nivoliens, Sylvain Lefebvre, and Bruno Lévy. Invisible seams. In *Computer Graphics Forum*, volume 29, pp. 1489–1496. Wiley Online Library, 2010.
- Pedro V Sander, Steven J Gortler, John Snyder, and Hugues Hoppe. Signal-specialized parametrization. In *Rendering Techniques*, pp. 87–98, 2002.
- Lior Shapira, Ariel Shamir, and Daniel Cohen-Or. Consistent mesh partitioning and skeletonisation using the shape diameter function. *The Visual Computer*, 24(4):249–259, 2008.
- Alla Sheffer and John C Hart. Seamster: inconspicuous low-distortion texture seam layout. In *IEEE Visualization, 2002. VIS 2002.*, pp. 291–298. IEEE, 2002.
- Alla Sheffer, Bruno Lévy, Maxim Mogilnitsky, and Alexander Bogomyakov. Abf++: fast and robust angle based flattening. *ACM Transactions on Graphics (TOG)*, 24(2):311–330, 2005.
- Alla Sheffer, Emil Praun, Kenneth Rose, et al. Mesh parameterization methods and their applications. *Foundations and Trends® in Computer Graphics and Vision*, 2(2):105–171, 2007a.
- Alla Sheffer, Emil Praun, Kenneth Rose, et al. Mesh parameterization methods and their applications. *Foundations and Trends® in Computer Graphics and Vision*, 2(2):105–171, 2007b.
- Jason Smith and Scott Schaefer. Bijective parameterization with free boundaries. *ACM Transactions on Graphics (TOG)*, 34(4):1–9, 2015.
- Olga Sorkine, Daniel Cohen-Or, Rony Goldenthal, and Dani Lischinski. Bounded-distortion piecewise mesh parameterization. In *IEEE Visualization, 2002. VIS 2002.*, pp. 355–362. IEEE, 2002.
- Pratul P Srinivasan, Stephan J Garbin, Dor Verbin, Jonathan T Barron, and Ben Mildenhall. Nuvo: Neural uv mapping for unruly 3d representations. In *European Conference on Computer Vision*, pp. 18–34. Springer, 2024.
- George Tang, William Zhao, Logan Ford, David Benhaim, and Paul Zhang. Segment any mesh. *arXiv preprint arXiv:2408.13679*, 2024.

- Fatemeh Teimury, Bruno Roy, Juan Sebastián Casallas, David MacDonald, and Mark Coates. Graphseam: Supervised graph learning framework for semantic uv mapping. *arXiv preprint arXiv:2011.13748*, 2020.
- William Thomas Tutte. How to draw a graph. *Proceedings of the London Mathematical Society*, 3(1):743–767, 1963.
- Eric Veach. *Robust Monte Carlo methods for light transport simulation*. Stanford University, 1998. URL [https://cseweb.ucsd.edu/~viscomp/classes/cse168/sp20/readings/veach\\_thesis.pdf](https://cseweb.ucsd.edu/~viscomp/classes/cse168/sp20/readings/veach_thesis.pdf).
- Jelle Vermandere, Maarten Bassier, and Maarten Vergauwen. Semantic uv mapping to improve texture inpainting for indoor scenes. *arXiv preprint arXiv:2407.09248*, 2024.
- Colin Weill-Duflos, David Coeurjolly, Fernando de Goes, and Jacques-Olivier Lachaud. Joint optimization of distortion and cut location for mesh parameterization using an ambrosio-tortorelli functional. *Computer Aided Geometric Design*, 105:102231, 2023.
- Fanbo Xiang, Zexiang Xu, Milos Hasan, Yannick Hold-Geoffroy, Kalyan Sunkavalli, and Hao Su. Neutex: Neural texture mapping for volumetric neural rendering. In *Proceedings of the IEEE/CVF Conference on Computer Vision and Pattern Recognition*, pp. 7119–7128, 2021.
- Baixin Xu, Jiangbei Hu, Fei Hou, Kwan-Yee Lin, Wayne Wu, Chen Qian, and Ying He. Parameterization-driven neural surface reconstruction for object-oriented editing in neural rendering. In *European Conference on Computer Vision*, pp. 461–479. Springer, 2024a.
- Tian-Xing Xu, Wenbo Hu, Yu-Kun Lai, Ying Shan, and Song-Hai Zhang. Texture-gs: Disentangling the geometry and texture for 3d gaussian splatting editing. In *European Conference on Computer Vision*, pp. 37–53. Springer, 2024b.
- Yaoqing Yang, Chen Feng, Yiru Shen, and Dong Tian. Foldingnet: Point cloud auto-encoder via deep grid deformation. In *Proceedings of the IEEE conference on computer vision and pattern recognition*, pp. 206–215, 2018.
- Qijian Zhang, Junhui Hou, and Ying He. Parapoint: Learning global free-boundary surface parameterization of 3d point clouds. *arXiv preprint arXiv:2403.10349*, 2024a.
- Qijian Zhang, Junhui Hou, Wenping Wang, and Ying He. Flatten anything: unsupervised neural surface parameterization. *Advances in Neural Information Processing Systems*, 37:2830–2850, 2024b.
- Yuming Zhao, Qijian Zhang, Junhui Hou, Jiazhi Xia, Wenping Wang, and Ying He. Flexpara: Flexible neural surface parameterization. *arXiv preprint arXiv:2504.19210*, 2025.
- Sergey Zhukov, Andrei Iones, and Grigoriy Kronin. An ambient light illumination model. In *Eurographics workshop on rendering techniques*, pp. 45–55. Springer, 1998.
- Guangyu Zou, Jiayi Hu, Xianfeng Gu, and Jing Hua. Authalic parameterization of general surfaces using lie advection. *IEEE Transactions on Visualization and Computer Graphics*, 17(12):2005–2014, 2011.

## A APPENDIX

### A.1 REMARKS ON SHAPE DIAMETER FUNCTION (SHDF)

Our semantic-aware parameterization, explained in Sec.3.3, relies on computing a per-vertex semantic partition of the input mesh using shape diameter function Shapira et al. (2008). To estimate per-vertex semantic label, we design and implement a method based on Shape Diameter Function Shapira et al. (2008) that involves the following key steps.

**Compute a per face local thickness (shape-diameter) field.** For a surface sample  $p$  (face centroid or vertex), the value  $\text{ShDF}(p)$  estimates the local object diameter by probing the interior along a cone centered on the inward normal at  $p$ . Let  $\mathcal{R}(p) = \{r_i\}_{i=1}^R$  be a set of rays radiating from  $p$  inside a cone of half-angle  $\alpha$  around the inward normal. For each ray  $r_i$  we compute the length  $\ell_i$  of the intersection segment between  $r_i$  and the mesh interior (i.e., the distance from  $p$  to the first opposite intersection). We robustly aggregate the ensemble  $\{\ell_i\}$  using a median (or trimmed mean) to obtain:  $\text{ShDF}(p) = \text{median}(\{\ell_i\}_{i=1}^R)$ . This median-based aggregation reduces sensitivity to spurious long or short intersections caused by complex local geometry. In practice, to estimate a scalar per surface element that measures local object thickness (intuitively, it presents the diameter of the object in the neighborhood of each sample), we use ray casting (using PyMeshLab Muntoni & Cignoni (2021)) in multiple directions per sample and return a per-face scalar. Then, the raw scalars are normalized to  $[0, 1]$  and re-scaled via a monotonic compression (e.g., a log-like transform) to reduce dynamic range and improve cluster separability. In our implementation we use per-face ShDF evaluated at face centroids with the following defaults: cone angle  $\theta = 120^\circ$  (as in the original work Shapira et al. (2008)), number of rays  $R = 60$ , and ray sampling distributed uniformly within the cone.

**Smoothing and normalization.** Similar to Shapira et al. (2008), we smooth raw ShDF samples on the mesh to promote spatial coherence and reduce pose-dependent noise. We apply a small number (e.g., 1-2) of iterations of Laplacian smoothing on the ShDF scalar field with area-weighted averaging. To balance values across scales and to boost contrast of small parts, we perform a normalization:

$$\tilde{\text{ShDF}}(p) = \frac{\log(1 + \text{ShDF}(p)) - \min_p \log(1 + \text{ShDF}(p))}{\max_p \log(1 + \text{ShDF}(p)) - \min_p \log(1 + \text{ShDF}(p))}. \quad (9)$$

**Fit a Gaussian Mixture Model (GMM) to ShDF values.** Given a desired number of semantic components, to obtain soft class probabilities, we fit a one-dimensional Gaussian mixture model (GMM) to the per-face thickness scalars obtained from previous step. The probabilities from the GMM provide a data-driven per-face likelihood for each component and serve as the unary data term in the subsequent energy formulation.

**Construct a boundary smoothness cost between adjacent faces.** To bias the partition toward spatially coherent regions, we compute a smoothness cost on adjacent face pairs based on local geometry (for example, a function of the dihedral angle). Intuitively, nearly-coplanar adjacent faces incur a low boundary penalty, whereas faces separated by sharp edges incur a higher penalty for being assigned the same label.

**Initial partition assignment via data likelihood.** As an initial labeling, each face is assigned to the GMM component with maximum probability (equivalently, minimum negative log-likelihood of the probability). This produces a purely data-driven segmentation that is generally noisy but captures the major mode structure of the thickness field.

**Refine partitioning via energy-based graph cuts.** The initial assignment, obtained from the previous step, is then refined using an iterative expansion-based graph-cut procedure that minimizes a global energy

$$E(\text{labeling}) = \sum_{\text{faces}} \mathcal{C}_{\text{data}}(\text{face}, \text{label}) + \sum_{\text{adjacent faces}} \mathcal{C}_{\text{smooth}}(\text{pair}) \cdot \mathbf{1}[\text{labels differ}], \quad (10)$$

where the unary term is derived from the GMM negative log-likelihoods and the pairwise term is the smoothness cost described above. The expansion moves are solved by an optimal min-cut on an auxiliary graph for each label. Repeating this process across labels and iterating a few times yields a stable and low-energy partition.

**Re-label connected components.** After refinement, a single label index can correspond to multiple disconnected components. To solve this issue, we relabel each connected component of faces so that

every final label corresponds to a single connected sub-mesh. This guarantees that subsequent per-part processing operates on contiguous regions.

**Post-processing.** To produce clean 3D segmentation results, we apply simple post-processing heuristics: (i) remove tiny components below a face-count threshold, (ii) smooth labels by majority filtering on local neighborhoods, and (iii) (when appropriate) merge adjacent labels that are semantically similar. These operations stabilize the partition and remove spurious tiny regions that would complicate per-part UV parameterization. The output is then a set of connected semantic sub-meshes  $\{\mathcal{M}_k = (V_k, F_k)\}_{k=1}^K$  suitable for the per-part UV parameterization stage described in Sec.3.2.

## A.2 REMARKS ON BASE ARCHITECTURE FOR UV-PARAMETERIZATION LEARNING

**Overview.** Our backbone, based on bi-directional cycle mapping proposed in Zhao et al. (2025), implements a learnable and interpretable pipeline that mimics the artist operations used to create a UV atlas: (i) *deforming network*, starting from a regular 2D grid of uniformly spaced coordinates, this network adaptively deforms the grid to produce a set of candidate UV coordinates that are potentially well-suited for mapping; (ii) *wrapping network*, this module maps 2D UV candidates, generated by the deforming network, to the 3D surface by smoothly bending and folding the deformed planar grid until it conforms to the target geometry (in this case the input 3D mesh) which leads to effectively bridge the 2D and 3D domains; (iii) *cutting network*, operating directly on the 3D surface, generated by the wrapping network, this network transforms the input closed 3D geometry, obtained from the wrapping network, into an open, more developable 3D surface manifold. By strategically determining seam locations, i.e. where to cut the input closed 3D surface, it facilitates distortion reduction in subsequent flattening steps; and (iv) *unwrapping network*, this final network projects the open 3D surface points back to the 2D domain, preserving smoothness and geometric coherence. In this design, each subnetwork is designed as a multilayer perceptron (MLP) applied pointwise to mesh vertices. The entire architecture is trained jointly in an end-to-end unsupervised fashion. The four subnetworks are assembled into two complementary branches that enforce both 2D-3D-2D and 3D-2D-3D cycle mappings, ensuring consistency across 2D and 3D domains. Coupled with differentiable loss functions designed to encourage bijectivity and minimize distortion, this backbone forms the base architecture of our method to achieve a candidate UV parameterization for the next stages. In the following, we detail on the loss designs and the interaction of the four sub-networks within the two-branch bi-directional cycle.

**Notation.** Let  $\mathcal{M} = (V, F)$  be a triangle mesh with vertex positions  $P \in \mathbb{R}^{V \times 3}$  and normals  $N \in \mathbb{R}^{V \times 3}$ . Let  $G = \{g_i\}_{i=1}^V \subset \mathbb{R}^2$  denote a canonical planar lattice (the artist’s canvas). The learnable UV mapping is  $u_\theta(\cdot)$ ; the four MLP sub-networks are *DeformNet*, *WrapNet*, *CutNet*, *UnwrapNet*.

**Sub-network Definitions.** Each module is implemented as a small pointwise MLP. We use additive residuals in the deform and cut modules to bias predictions toward small, interpretable offsets:

$$\widehat{Q} = \text{DeformNet}(G) = G + \phi_d''([\phi_d'(G); G]), \quad (11)$$

$$[\widehat{P}, \widehat{N}] = \text{WrapNet}(\widehat{Q}) = \phi_w''([\phi_w'(\widehat{Q}); \widehat{Q}]), \quad (12)$$

$$\widehat{P}_{\text{cut}} = \text{CutNet}(\widehat{P}) = \widehat{P} + \phi_c''([\phi_c'(\widehat{P}); \widehat{P}]), \quad (13)$$

$$\widehat{Q}_{\text{cycle}} = \text{UnwrapNet}(\widehat{P}_{\text{cut}}) = \phi_u(\widehat{P}_{\text{cut}}). \quad (14)$$

where  $\widehat{Q}$  are deformed 2D candidates,  $\widehat{P}$  are wrapped 3D points (with normals  $\widehat{N}$ ),  $\widehat{P}_{\text{cut}}$  is the opened 3D surface after the learned cut offsets,  $\widehat{Q}_{\text{cycle}}$  are the re-flattened coordinates produced by the UnwrapNet,  $\phi_d'' : \mathbb{R}^{(h+2)} \rightarrow \mathbb{R}^2$ ,  $\phi_d' : \mathbb{R}^2 \rightarrow \mathbb{R}^h$ ,  $\phi_w' : \mathbb{R}^2 \rightarrow \mathbb{R}^h$ ,  $\phi_w'' : \mathbb{R}^{h+2} \rightarrow \mathbb{R}^6$ ,  $\phi_c'' : \mathbb{R}^{h+3} \rightarrow \mathbb{R}^3$ ,  $\phi_c' : \mathbb{R}^3 \rightarrow \mathbb{R}^h$ , and  $\phi_u : \mathbb{R}^3 \rightarrow \mathbb{R}^2$  are implemented as stacked MLP layers.

**Sub-network architectures.** Each subnetwork is implemented as a sequence of PWE blocks (pointwise  $1 \times 1$  convolution with LeakyReLU activation functions), applied point-wisely to per-vertex features. In practice each MLP is split into an encoding stage (MLP\_1) and a decoding stage (MLP\_2) (e.g., Deform use  $[2 \rightarrow 512 \rightarrow 512 \rightarrow 512 \rightarrow 64]$  then  $[66 \rightarrow 512 \rightarrow 512 \rightarrow 512 \rightarrow 2]$  as encoder and decoder, respectively). DeformNet produces deformed UV candidates, WrapNet maps those

Table 3: Layer-wise summary of four sub-networks used in our base neural UV architecture (PWE = point-wise embedding conv1d). Each listed MLP is a sequence of PWE blocks; intermediate PWEs use LeakyReLU (with the negative slope of 0.01) while the final PWE is linear.

Subnetwork	Component	Layer channels	# PWE	Input / Output dim	Notes (activation)
DeformNet	MLP.1	[2 → 512 → 512 → 512 → 64]	4	2 / 64	LeakyReLU(0.01) on hidden PWEs; final PWE linear
	MLP.2	[66 → 512 → 512 → 512 → 2]	4	66 / 2	LeakyReLU(0.01) on hidden PWEs; final PWE linear
WrapNet	MLP.1	[2 → 512 → 512 → 512 → 64]	4	2 / 64	same as Deform MLP.1
	MLP.2	[66 → 512 → 512 → 512 → 6]	4	66 / 6	outputs 6D (3 coords + 3 normals)
CutNet	MLP.1	[3 → 512 → 512 → 64]	3	3 / 64	LeakyReLU(0.01) on hidden PWEs; final PWE linear
	MLP.2	[67 → 512 → 512 → 3]	3	67 / 3	produces 3D offsets $X_o$ (then $X_c = X + X_o$ )
UnwrapNet	MLP	[3 → 512 → 512 → 2]	3	3 / 2	maps cut 3D points → 2D unwrapped points
	CutNet	see above	—	3 / 3	Unwrapping uses Cutting before this MLP
PWE (block)	conv layer	Conv1d(kernel=1); $C_{in} \rightarrow C_{out}$	1 (per call)	-	point-wise 1D conv + bias; optional LeakyReLU(0.01)

2D candidates to 3D points and normals, CutNet predicts pointwise 3D offsets to open the surface (making it more developable), and UnwrapNet applies CutNet followed by a final MLP to project the opened surface back to 2D. All subnetworks operate pointwise (per-vertex), the final PWE in each MLP is linear, intermediate PWEs use LeakyReLU as activation functions, and the entire architecture is trained end-to-end in an unsupervised manner (see Table 3 for a layer-wise breakdown).

**Bi-Directional Cycle Mapping.** We follow Zhang et al. (2024b); Srinivasan et al. (2024); Zhao et al. (2025) to build our base neural UV parameterization architecture with two-branch MLP architecture that leverages the four sub-networks, explained above.

- **2D-3D-2D:**  $G \xrightarrow{DeformNet} \hat{Q} \xrightarrow{WrapNet} \hat{P} \xrightarrow{CutNet} \hat{P}_{cut} \xrightarrow{UnwrapNet} \hat{Q}_{cycle}$ . Enforcing  $\hat{Q}$  to be close to  $\hat{Q}_{cycle}$  stabilizes deformations and ensures that the learned 2D deformations are actually realizable on the surface.
- **3D-2D-3D:**  $P \xrightarrow{CutNet} P_{cut} \xrightarrow{UnwrapNet} Q \xrightarrow{WrapNet} \tilde{P}$ . Enforcing  $\tilde{P}$  to be close to  $P$  constrains the unwrapping map so that the predicted UV coordinates can be re-embedded to match the true geometry.

Together the two cycles expose inconsistencies including any seams, overlaps, stretches, and/or distortions as reconstruction losses that the network can reduce. We now detail all the reconstruction losses in detail.

**Training losses.** The backbone is trained with a weighted sum of unsupervised, geometry-aware losses:

$$\mathcal{L} = \lambda_{wrap} \mathcal{L}_{wrap} + \lambda_{cycle} \mathcal{L}_{cycle} + \lambda_{repel} \mathcal{L}_{repel} + \lambda_{dist} \mathcal{L}_{dist} \quad (15)$$

Below are the main terms.

**Wrapping loss.** Encourages  $\hat{P}$  (Wrap-Net output) to approximate the input surface by computing the chamfer distance between the input mesh vertices  $P$  and reconstructed  $\hat{P}$ :

$$\mathcal{L}_{wrap} = \text{ChamferDistance}(\hat{P}, P) + \kappa_{norm} (1 - \text{CosineSim}(\hat{N}, N)) \quad (16)$$

where the second term enforces vertex normal consistency by computing point-wise cosine similarity between normal vectors.

**Cycle-consistency loss.** Penalizes reconstruction error on both cycles by computing the squared norm 2 of the pair of deformed 2D candidates  $\hat{Q}$  and the output of UnwrapNet  $\hat{Q}_{cycle}$  and the pair of input mesh vertices  $P$  and reconstructed vertices  $\hat{P}$  from the WrapNet:

$$\mathcal{L}_{cycle} = \|\hat{Q} - \hat{Q}_{cycle}\|_2^2 + \|P - \tilde{P}\|_2^2 \quad (17)$$

optionally augmented with normal/feature consistency terms.

**Anti-overlap (repulsion).** Discourages UV overlaps by repelling nearby vertex pairs in UV space:

$$\mathcal{L}_{\text{repe}} = \frac{1}{|\mathcal{N}|} \sum_{(i,j) \in \mathcal{N}} \phi(\|u_{\theta}(i) - u_{\theta}(j)\|_{\text{uv}}) \quad (18)$$

where  $\mathcal{N}$  denotes local neighbor pairs,  $\phi$  is a hinge-style repulsion, and  $\|\cdot\|_{\text{uv}}$  includes chart-periodicity handling.

**Differential and triangle distortion losses.** Control conformal and area distortion using a Jacobian-level differential loss (DDL) and a triangle-based discrete loss (TDL):

$$\mathcal{L}_{\text{dist}} = \lambda_{\text{DDL}} \mathcal{L}_{\text{DDL}} + \lambda_{\text{TDL}} \mathcal{L}_{\text{TDL}} \quad (19)$$

The DDL is computed by applying automatic differentiation to the MLP outputs to approximate the local Jacobian, while the TDL explicitly measures changes in angles and areas between 3D triangles and their corresponding 2D counterparts. In practice, we adopt the same formulations of DDL and TDL as proposed in Zhao et al. (2025), and refer readers to Sheffer et al. (2007b); Hormann et al. (2007); Floater & Hormann (2005) for further details on distortion metrics and differential geometry concepts.

### A.3 ADDITIONAL EXPERIMENTS AND RESULTS

We show expanded results, ablation studies, and discussions from the main paper featuring more surface parameterization and more viewpoints of different 3D objects in Figs. 7- 14, and Tables. 4 and 5.

**Additional Ablation Studies.** In addition to the ablations reported in the main text, we further ablate the full framework by training identical models with and without the semantic and/or visibility objectives. Results in Table 5 show that adding semantic and/or visibility objectives to the base geometry-preserving UV parameterization model (Sec. 3.2 and Appendix A.2) preserves the model’s geometry-preserving properties: any loss in conformality or area preservation is minor. Also, these small quantitative degradations do not harm perceptual quality. Specifically, qualitative comparisons throughout the paper show the textured results remain competitive with baselines, despite slight drops in some numerical metrics.

Table 4: Ablation studies on the proposed partitioning strategy (ShDF vs. SAMesh). We replace our default Shape Diameter Function (ShDF) partitioner Shapira et al. (2008) with SAMesh Tang et al. (2024) while keeping the remainder of the *partition-and-parameterize* pipeline identical. Quantitatively, using ShDF in our pipeline yields UV parameterizations that are more conformal (better angle preservation) and more equiareal (better area preservation) than those produced when using SAMesh.

Method	Conformality $\uparrow$	Equiareality $\uparrow$
Ours - Semantic-Aware Param (SAMesh)	0.8694	0.6270
Ours - Semantic-Aware Param (ShDF)	<b>0.9123</b>	<b>0.6707</b>

Table 5: Ablation: effect of semantic and visibility objectives on geometry-preserving metrics. Reported are mean Conformality and Equiareality (higher is better). The numbers show that adding semantic and/or visibility objectives to the base neural UV architecture causes only minor changes in these geometry-preserving metrics while improving perceptual/qualitative behavior.

Method	Conformality $\uparrow$	Equiareality $\uparrow$
Base Neural UV Arch.	0.9097	<b>0.6759</b>
Ours - Semantic-Aware Param	0.9123	0.6707
Ours - Visibility-Aware Param	<b>0.9175</b>	0.6093
Ours - Visibility+Semantic-Aware Param	0.9153	0.6369

## B THE USE OF LARGE LANGUAGE MODELS

We used a large language model (LLM) to assist with editing, refining, and polishing the manuscript text (for example: abstract and captions). The LLM was used only for language refinement, improving grammar, wording, concision, and overall readability, and did not contribute to the technical

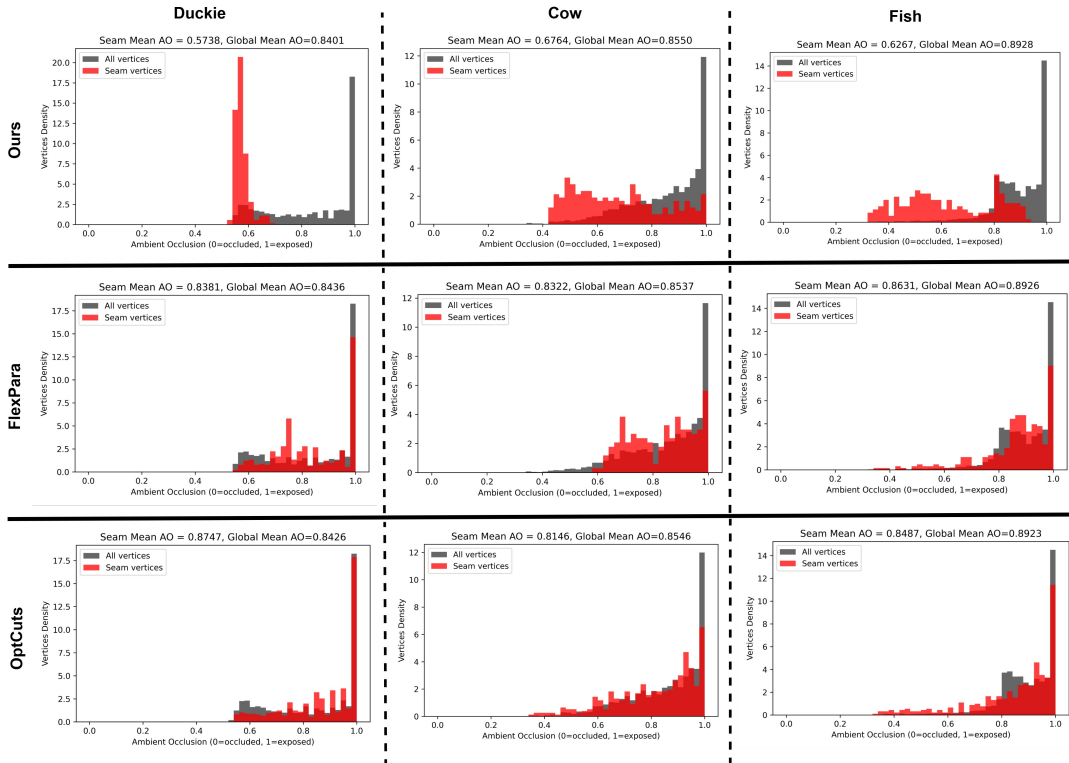


Figure 7: Quantitative distribution of seam-vertex ambient occlusion (AO) for three meshes parameterized with our method, FlexPara Zhao et al. (2025), and OptCuts Li et al. (2018). Red bars indicate AO distributions of seam vertices, while black bars represent all vertices. The  $y$ -axis denotes vertex density and the  $x$ -axis AO values. Our method shifts seam-vertex AO distributions toward lower values (left side), showing that the visibility-aware pipeline relocates seams to less visible (more occluded) regions, unlike FlexPara and OptCuts.

content, experiments, results, or scientific claims. All suggestions generated by LLM were manually and carefully reviewed and, where appropriate, revised by the authors. The authors have full responsibility for the final text and for the accuracy of the work.

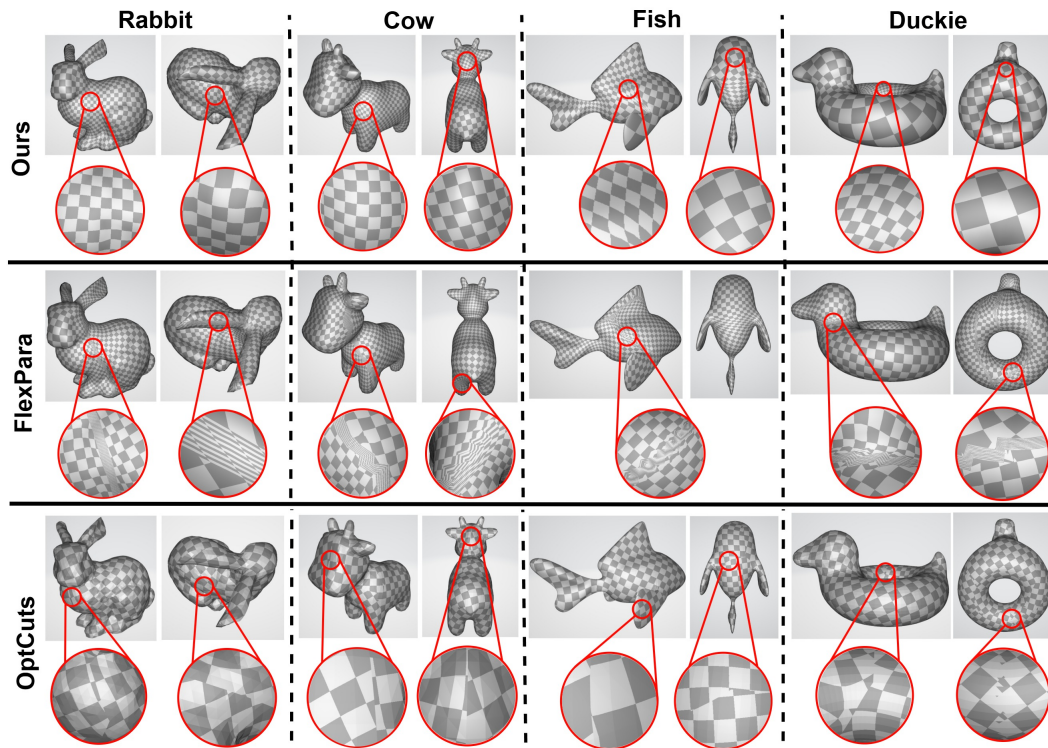


Figure 8: Extended version of Fig. 5 in the main paper. Checkerboard texturing comparison using UV parameterizations produced by our visibility-aware method, FlexPara Zhao et al. (2025), and OptCuts Li et al. (2018). Each row shows rendered views of different meshes textured with a checkerboard and a magnified inset of a visually important region near seams (red circles). Because our method steers seams toward occluded regions, the checkerboard pattern appears substantially more continuous from typical camera viewpoints. By contrast, baselines exhibit visible seam artifacts in the zoomed-in insets.

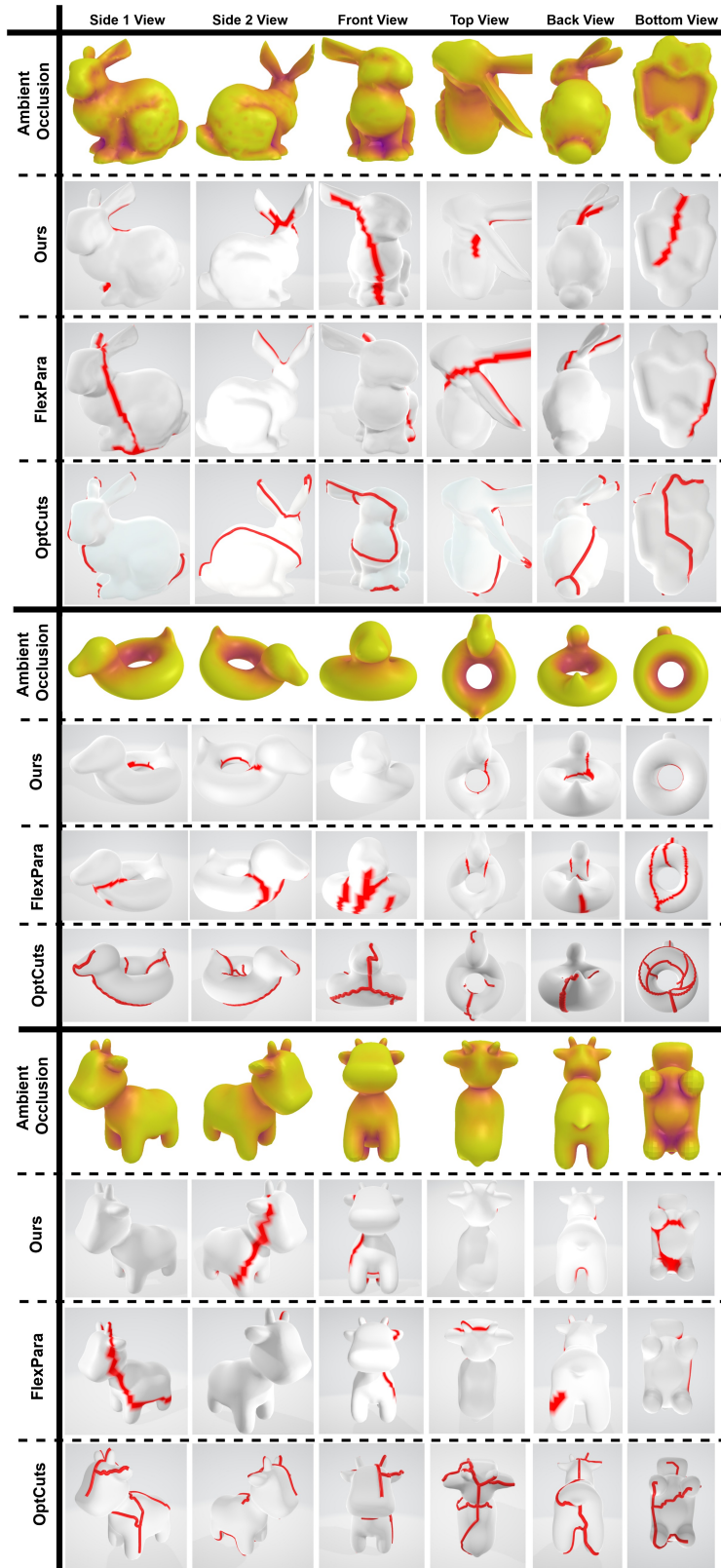


Figure 9: Extended version of Fig. 4 in the main paper. Qualitative results for visibility-aware seam placement and UV parameterization on three representative meshes. For each mesh, the top row shows per-vertex ambient occlusion (yellow = exposed, purple = occluded). Beneath are the visualizations of cutting seams (red) from our method, FlexPara Zhao et al. (2025), and OptCuts Li et al. (2018) (top to bottom). Our method places a larger fraction of seam geometry in less-exposed regions, reducing the likelihood of visible seam artifacts under typical viewpoints.

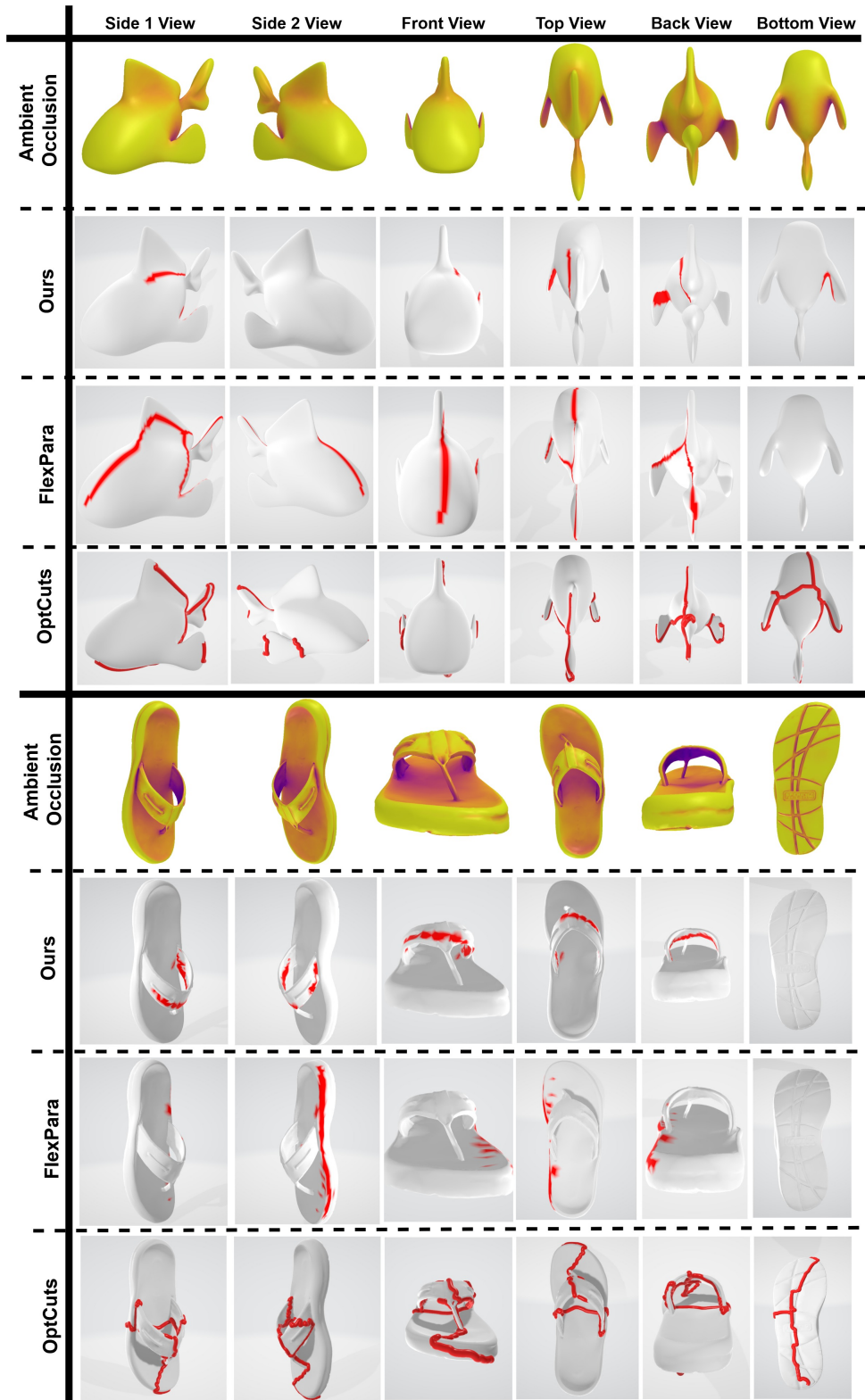


Figure 10: Extended version of Fig. 4 in the main paper. Qualitative results for visibility-aware seam placement and UV parameterization on three representative meshes. For each mesh, the top row shows per-vertex ambient occlusion (yellow = exposed, purple = occluded). Beneath are the visualizations of cutting seams (red) from our method, FlexPara Zhao et al. (2025), and OptCuts Li et al. (2018) (top to bottom). Our method places a larger fraction of seam geometry in less-exposed regions, reducing the likelihood of visible seam artifacts under typical viewpoints.

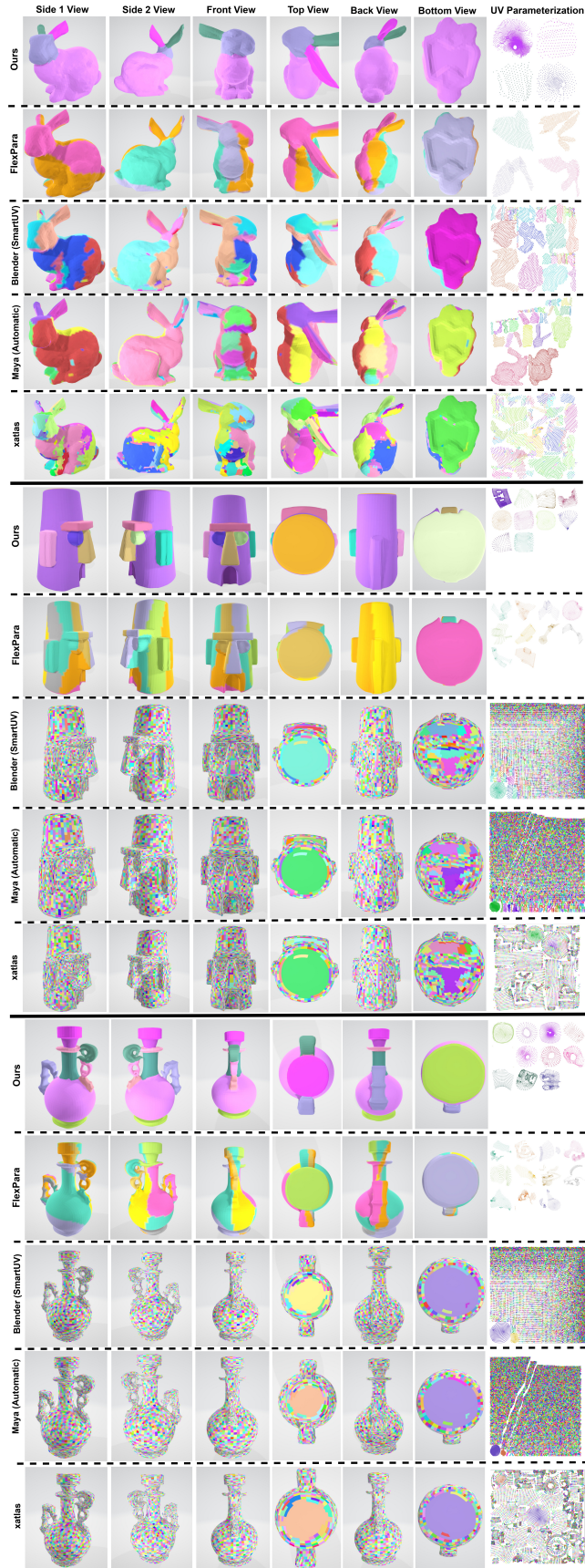


Figure 11: Extended version of Fig. 3 in the main paper. Qualitative results of the proposed semantic-aware UV parameterization method on a Rabbit mesh. For each method, we show the rendered 3D objects from multiple viewpoints, with the corresponding UV atlas in the rightmost column. As shown, our method produces UV charts that align more semantically with the mesh’s 3D semantic parts, unlike the baselines.

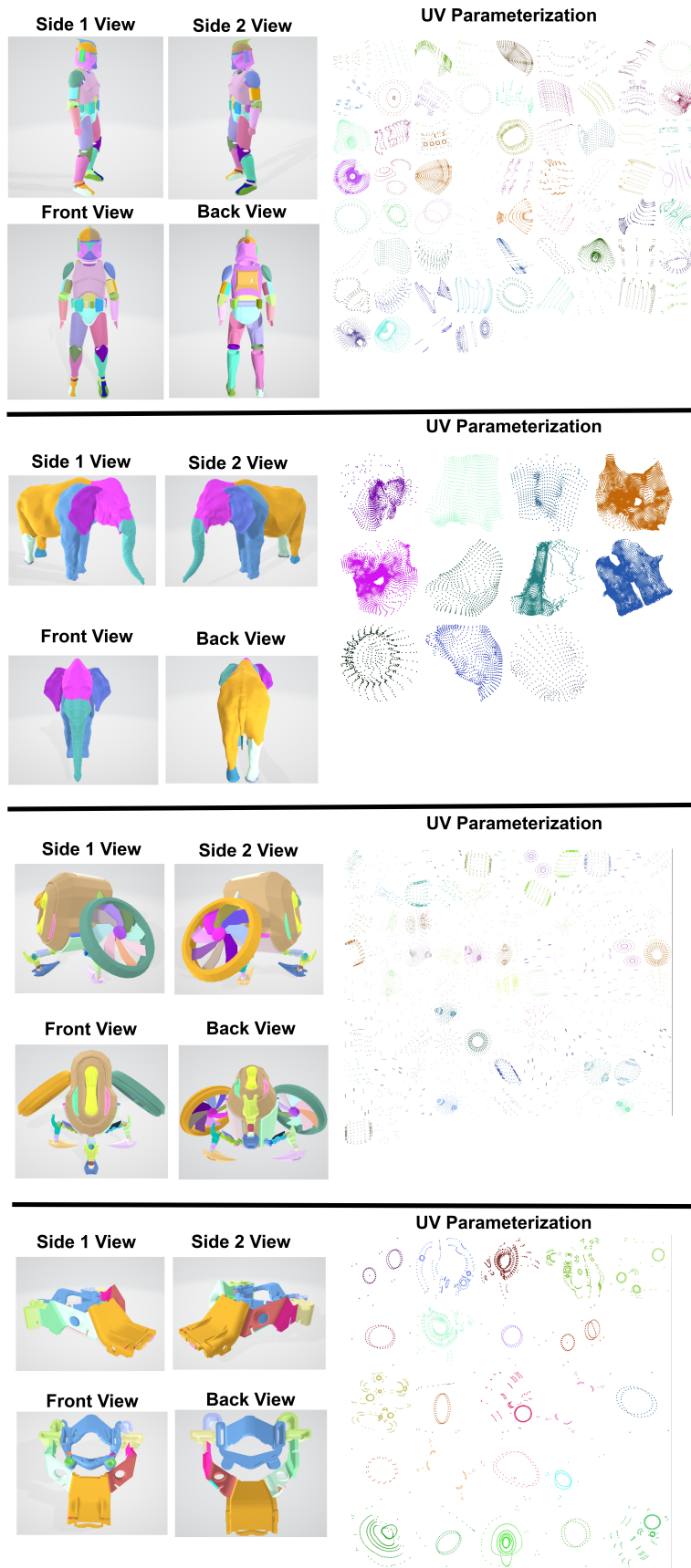


Figure 12: Qualitative results of the proposed semantic-aware UV parameterization method on complex mesh objects with high number of triangle faces. For each method, we show the rendered 3D objects from multiple viewpoints, with the corresponding UV atlas in the rightmost column. As shown, our method is able to produce UV charts, for complex meshes, that are align more semantically with the mesh's 3D semantic parts

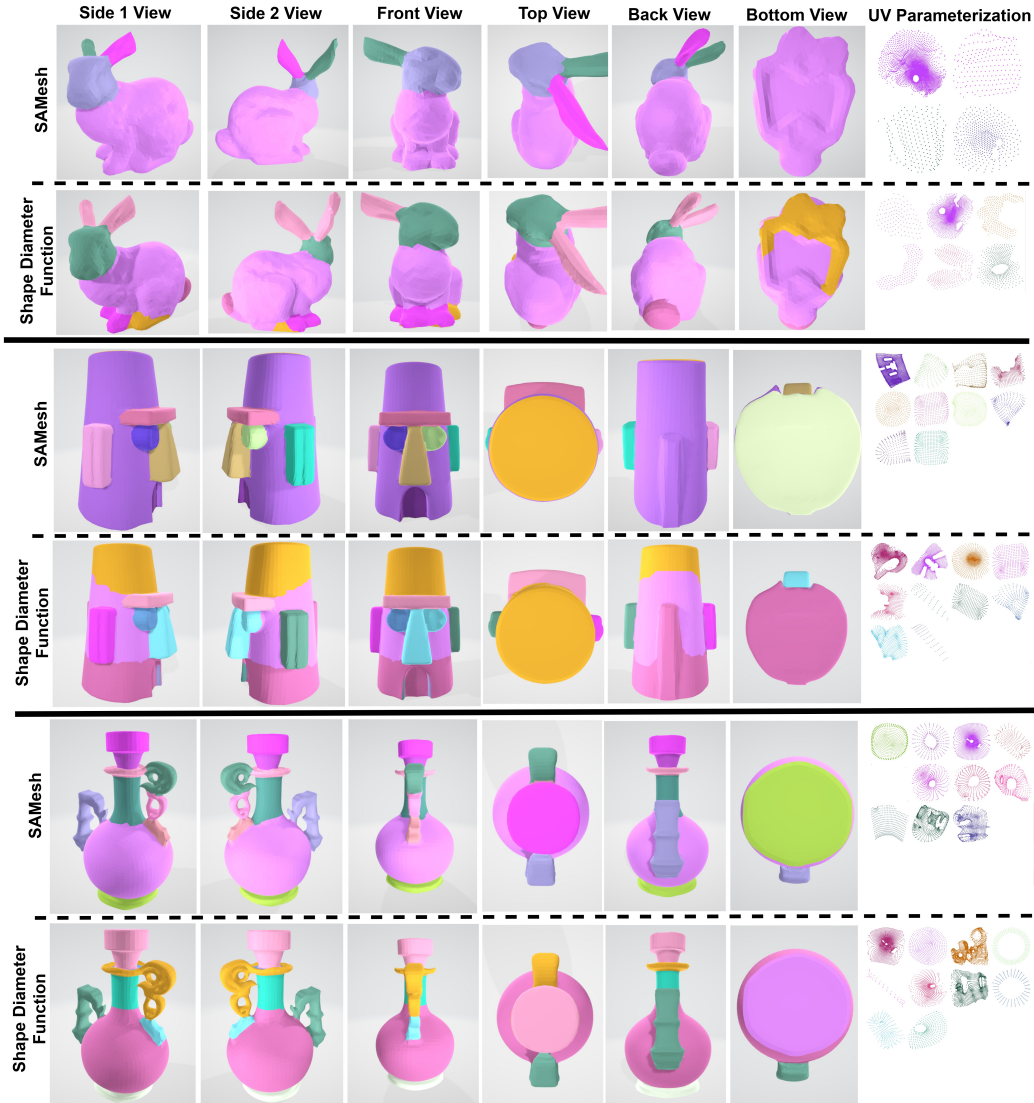


Figure 13: Ablation studies on the proposed partitioning strategy (ShDF vs. SAMesh) of simple meshes. We replace our default Shape Diameter Function (ShDF) partitioner Shapira et al. (2008) with SAMesh Tang et al. (2024) while keeping the remainder of the *partition-and-parameterize* pipeline identical. Qualitatively both partitioners produce part decompositions that align with geometric structure across simple and complex models, resulting in compact, low-distortion per-part UV charts.

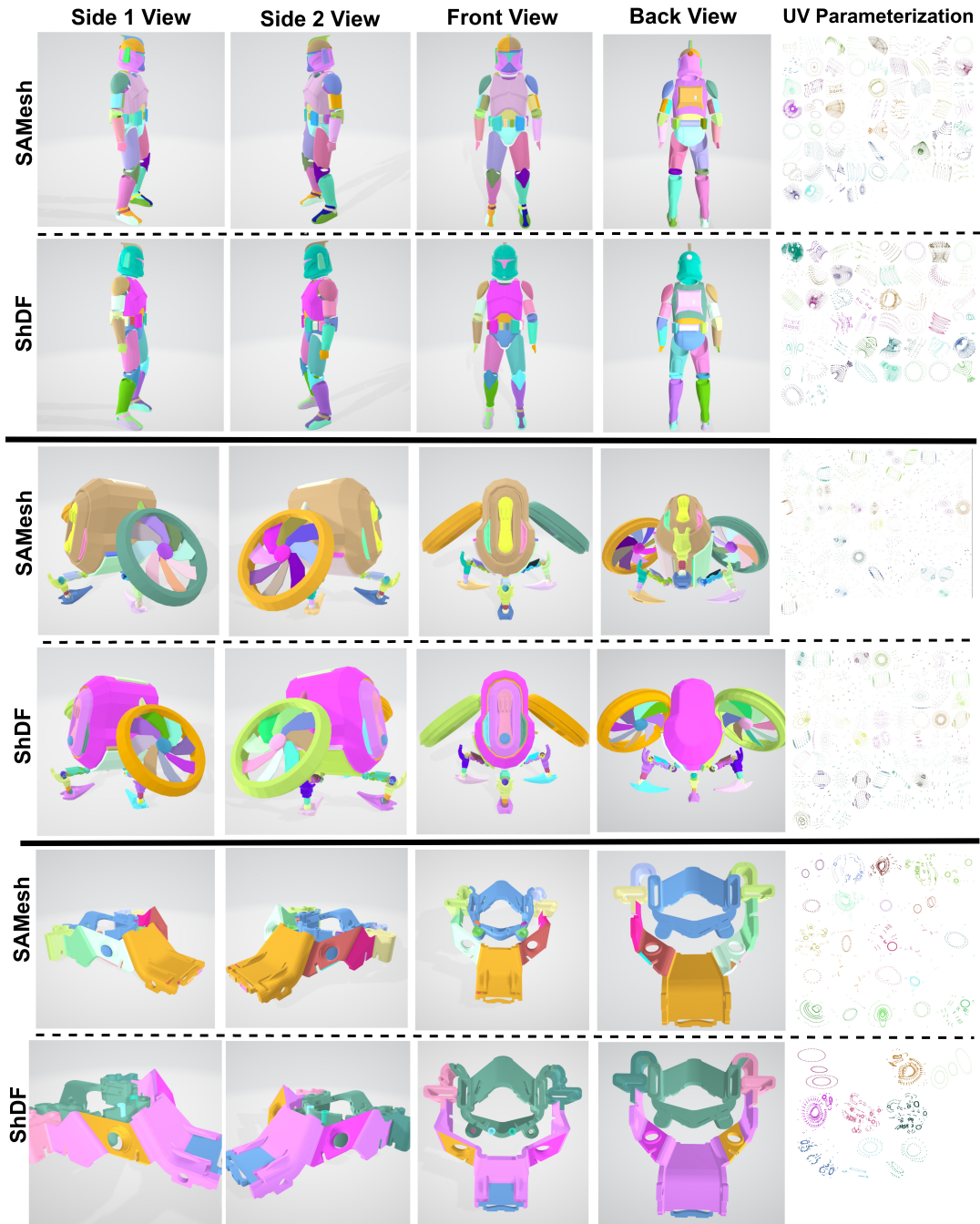


Figure 14: Ablation studies on the proposed partitioning strategy (ShDF vs. SAMesh) of complex meshes with high number of triangle faces. We replace our default Shape Diameter Function (ShDF) partitioner Shapira et al. (2008) with SAMesh Tang et al. (2024) while keeping the remainder of the *partition-and-parameterize* pipeline identical. Qualitatively both partitioners produce part decompositions that align with geometric structure across simple and complex models, resulting in compact, low-distortion per-part UV charts.